DUMoE: Deep Unfolding Mixture-of-Experts for Compressive Imaging

Anonymous authors
Paper under double-blind review

Abstract

Deep Unfolding-based Networks (DUNs) have attracted attention due to their high performance and a certain degree of interpretability. However, existing DUNs often lack flexibility in handling details and features in different images during reconstruction, as they typically involve multiple iterative modules cascading through the same structure for each iteration. To address this limitation, we propose DUMoE, a novel sparsely-activated Deep Unfolding Mixture-of-Experts (MoE) architecture for Compressive Imaging (CI). By integrating the deep unfolding paradigm into the MoE, we enable DUMoE to adaptively reconstruct various images by utilizing different experts at each iteration stage. Specifically, we unfold traditional SpaRSA iterations into experts within DUMoE and employ top-1 switch routing to save computational consumption and enhance flexibility. Additionally, we introduce the Degradation-Aware Mask within the self-attention mechanism to prioritize image degradation caused by dimensionality reduction in CI, thereby enhancing reconstruction fidelity. Moreover, we incorporate the Multi-Scale Gate to improve the DUMoE's adaptability to image features at different scales and facilitate information transmission across iteration stages. Extensive experiments across various CI recovery tasks, including natural image compressive sensing, magnetic resonance imaging, and snapshot compressive imaging, demonstrate the superior performance and effectiveness of DUMoE. To the best of our knowledge, we are the first to leverage the deep unfolding paradigm within the MoE framework.

1 Introduction

Compressive Imaging (CI) is an imaging methodology that leverages signal sparsity or compressibility principles to enable high-fidelity image reconstruction using markedly fewer samples than conventional methods (Candès & Wakin (2008)). This capability allows CI to dramatically reduce sampling complexity and data storage requirements, while concurrently enhancing imaging speed and efficacy. Therefore, CI finds extensive applications across diverse domains, particularly in natural Image Compressive Sensing (ICS) (Kulkarni & Turaga (2015); Zhang & Ghanem (2018); Zha et al. (2023)), CS Magnetic Resonance Imaging (CS-MRI) (Lustig et al. (2007; 2008); Yang et al. (2016)), and Snapshot Compressive Imaging (SCI) (Ma et al. (2019); Yuan et al. (2021); Cheng et al. (2023)). Specifically, assuming that $\mathbf{x} \in \mathbb{R}^N$ denotes the vector of representation coefficients of original signal, $\mathbf{A} \in \mathbb{R}^{M \times N} (M \ll N)$ denotes the linear sampling matrix, and $\mathbf{y} \in \mathbb{R}^M$ is the measurement obtained from underdetermined system $\mathbf{y} = \mathbf{A}\mathbf{x}$, traditional CI recovery problem can be formulated as follows:

$$\min_{\mathbf{x}} \frac{1}{2} \|\mathbf{A}\mathbf{x} - \mathbf{y}\|_{\ell_2}^2 + \tau \mathcal{R}(\mathbf{x}), \tag{1}$$

Existing methods for CI recovery problem can be classified into three categories: traditional optimization methods, purely Deep Learning (DL)-based networks, and Deep Unfolding-based Networks (DUNs). First, traditional optimization methods, such as Iterative Shrinkage/Thresholding Algorithm (ISTA) (Beck & Teboulle (2009)), Alternating Direction Method of Multipliers (ADMM) (Boyd (2010)), Fixed-Point Continuation (FPC) (Hale et al. (2008)), Sparse Reconstruction by Separable Approximation (SpaRSA) (Wright et al. (2009)), and others (Bioucas-Dias & Figueiredo (2007); Goldstein & Osher (2009); Chambolle & Pock (2011); Donoho et al. (2009)), typically rely on iterative steps to gradually optimize results and achieve (sub)optimal outcomes with theoretical guarantees. However, these methods often require hand-crafted parameters fine-tuning, exhibit

limited representation ability across various data, and demand significant computational time to attain satisfactory results. Second, purely DL-based networks (Kulkarni et al. (2016); Gan et al. (2023a;b); Shen et al. (2024)) leverage DL modules such as convolutional neural networks (CNNs), Vision Transformer (ViT) (Dosovitskiy et al. (2021)), and their combinations to learn the mapping relationship between measurements and ground truth images, thus achieving superior reconstruction performance. However, these methods do not possess theoretically proven properties and interpretability, as they often lack insights and knowledge from the CI domain. Third, DUNs (Zhang & Ghanem (2018); Gan et al. (2024b); Yang et al. (2020)) are inspired by traditional iterative optimization algorithms like ISTA, ADMM and FPC. They integrate DL modules into the iterative steps of these optimization algorithms, creating cascaded networks with multiple stages, where each stage represents an iteration within the optimization algorithm. This integration not only leads to fast and accurate CI recovery but also introduces domain-specific prior knowledge inherent to the CI domain.

However, existing DUNs often employ multiple iterative modules cascading through the same module for each iteration, limiting flexibility when handling fine-grained details in diverse images. To overcome this limitation, we propose DUMoE, a sparsely-activated Deep Unfolding Mixture-of-Experts (MoE) framework for CI tasks. Initially, we transform the iterative steps of the SpaRSA algorithm into deep unfolding modules, integrating them as experts within DUMoE. During reconstruction, rather than utilizing all experts, we adopt the top-1 switch routing, thereby reducing computational overhead and enhancing the model's flexibility to handle details and features in distinct images. Additionally, we introduce the Degradation-Aware Mask into the self-attention mechanism to enhance DUMoE's focus on image areas susceptible to degradation in various CI tasks. Furthermore, we integrate U-Block into the Gate modules to leverage multi-scale features for experts selection and enhanced image reconstruction, and improve feature transmission during the reconstruction.

Our contributions can be summarized as follows:

(i) We propose DUMoE, a novel sparse MoE framework integrated with deep unfolding SpaRSA. Within DUMoE, we unfold the iterations of traditional SpaRSA into experts, i.e., Deep Unfolding SpaRSA Experts, which are sparsely-activated based on the top-1 switch routing. To the best of our knowledge, we are the first to leverage the deep unfolding paradigm within the MoE framework, yielding state-of-the-art (SOTA) results across various CI tasks.

(ii) We introduce the Degradation-Aware Mask within the self-attention mechanism of DUMoE, enhancing its adaptability to image degradation in diverse CI tasks. This refinement allows DUMoE to focus more attentively on degraded image details, resulting in higher-quality reconstructed images.

(iii) We incorporate a Multi-Scale Gate into DUMoE, which enhances the capacity of model to capture fine-grained feature across different image scales, and facilitates the transmission of multi-scale features at different stages, leading to significant improvements in reconstruction performance.

Comprehensive comparative analyses between DUMoE and other SOTA methods across ICS, CS-MRI, and SCI, highlight the excellent performance of our proposed DUMoE, demonstrating its effectiveness in various CI tasks.

2 Related Works

In recent, various DUNs have emerged in the fields of ICS, CS-MRI, and SCI, showing significant advancements in image reconstruction. In ICS, researchers have devised DUNs to reconstruct natural images from limited measurements. For instance, Zhang and Ghanem introduced ISTA-Net$^+$ (Zhang & Ghanem (2018)), which integrates CNNs into ISTA's iterative steps and utilizes them for sparse transform-related proximal mapping. Besides, based on the FPC algorithm, Wang and Gan proposed UFC-Net (Wang & Gan (2024)), which introduces the convolution-guided attention and auxiliary iterative reconstruction block to enhance feature extraction and preservation. Other methods include DPC-DUN (Song et al. (2023b)), NesTD-Net (Gan et al. (2024a)), and LTwIST (Gan et al. (2024b)), among others (Chen & Zhang (2022); Zhang et al. (2020); You et al. (2021); Chen et al. (2022); Mou et al. (2022); Song et al. (2023a); Chen et al. (2023a); Song et al. (2023c); Song & Zhang (2023)). In CS-MRI, methods like ADMM-CSNet (Yang et al. (2020)), HiTDUN (Zhang et al. (2022)), MAPUN (Song et al. (2023a)), along with others (Zhang & Ghanem (2018); Neyra-Nesterenko & Adcock (2022); Gan et al. (2024b;a); Wang & Gan (2024)) have been developed to reconstruct high-quality images from partial Fourier data, enabling faster imaging and reduced data acquisition. ADMM-

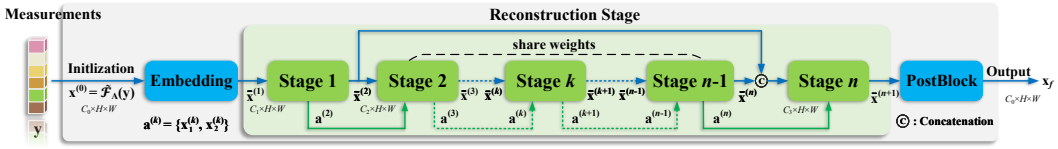

Figure 1: The overall structure of DUMoE. DUMoE contains an embedding block, n iteration stages, and a post-block. Here, $\mathbf{y}$ represents the measurement and $\mathbf{x}_f$ denotes the output of DUMoE.

CSNet (Yang et al. (2020)) unfolds and generalizes the ADMM algorithm into a deep architecture, while HiTDUN (Zhang et al. (2022)) facilitates multichannel information transmission between unfolding iterative stages. In the domain of SCI, methods like ADMM-Net (Ma et al. (2019)), DGSMP (Huang et al. (2021)), GAP-Net (Meng et al. (2023)), and others (Cai et al. (2022c); Li et al. (2023b); Dong et al. (2023); Qin et al. (2024); Zhao et al. (2024)), aim to recover 3D hyperspectral images (HSI) from 2D measurements containing spectral channel information. For example, Ma et al. proposed ADMM-Net (Ma et al. (2019)), which transforms the ADMM algorithm into a layerwise structure to learn the sparse representation domain through network training. Besides, Meng et al. introduced GAP-Net (Meng et al. (2023)), which unfolds the generalized alternating projection (GAP) algorithm, utilizing CNNs as denoisers projecting the estimate back to the desired signal space.

Recently, Mixture-of-Experts (MoE) has garnered considerable attention in both Natural Language Processing (Shazeer et al. (2017); Dryden & Hoefler (2022); Fedus et al. (2022); Zoph et al. (2022); Mustafa et al. (2022)) and Computer Vision (Riquelme et al. (2021); Puigcerver et al. (2022); Li et al. (2023a); Chen et al. (2023b); Wang et al. (2023); Ye & Xu (2023)). Typically, an MoE layer comprises many experts sharing the same network architecture, alongside a sparse gating or routing function that directs individual inputs to the top-K experts among all candidates (Shazeer et al. (2017); Fedus et al. (2022)). This approach only requires the computation of K experts for a new input, resulting in fast inference times. For instance, Williams et al. introduced the Switch Transformer (Fedus et al. (2022)), a model with sparsely-activated experts, which replaces the dense feed-forward network (FFN) layer in the Transformer with a sparse Switch FFN layer and enables stability in the training process of large sparse models.

3 Proposed Method

3.1 Sampling Process

Different CI tasks involve diverse sampling processes. Thus, we offer a broad overview here, with detailed task-specific descriptions in Appendix A.2. Let $\mathcal{F}_{\mathbf{A}}(\cdot)$ denote the sampling function and $\mathbf{x}$ be the original images. The generalized sampling process can be formulated as:

$$\mathbf{y} = \mathcal{F}_{\mathbf{A}}(\mathbf{x}), \tag{2}$$

where $\mathbf{y}$ denotes the obtained measurement derived from $\mathbf{x}$.

3.2 Reconstruction Stage

As shown in Fig. 1 and Fig. 2, the reconstruction stage includes an embedding module, n iteration stages and a post-block. First, assuming $\widetilde{\mathcal{F}}_{\mathbf{A}}(\cdot)$ represents the initialization function, the process of obtaining an initial estimate $\mathbf{x}^{(0)} \in \mathbb{R}^{C_0 \times H \times W}$ from the measurement $\mathbf{y}$ can be expressed as:

$$\mathbf{x}^{(0)} = \widetilde{\mathcal{F}}_{\mathbf{A}}(\mathbf{y}), \tag{3}$$

where C_0 denotes the basic channel count, set to 1 for images in ICS and CS-MRI tasks, and 28 for SCI tasks. The embedding module starts with a 3×3 convolution to increase the channel count from C_0 to C_1, followed by a Depth-wise Channel Attention Block (DCAB). The post-block structure mirrors that of the embedding module, albeit in reverse order. Each iteration stage integrates Degradation-Aware Self-Attention, Multi-Scale Gate, and three Deep Unfolding SpaRSA Experts. In the first stage, the channel count is C_1, while from the 2-nd to the $(n-1)$-th stage, it is C_2, with weights shared across them. Moreover, the channel count of n-th iteration stage is $C_3 = C_1 + C_2$.

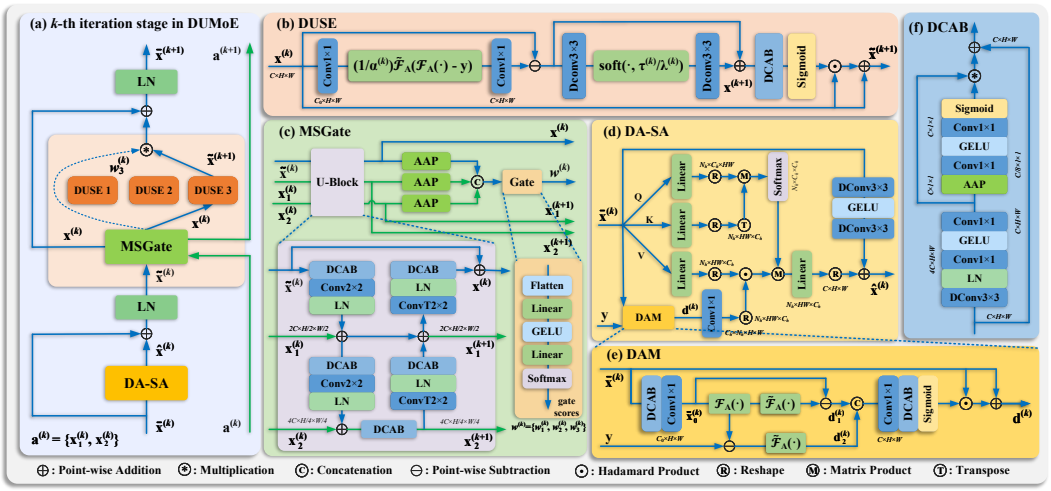

Figure 2: Detailed structure of DUMoE: (a) The k-th iteration stage in DUMoE; (b) Deep Unfolding SpaRSA Experts (DUSE); (c) Multi-Scale Gate (MSGate); (d) Degradation-Aware Self-Attention (DA-SA); (e) Degradation-Aware Mask (DAM); (f) Depth-wise Channel Attention Block (DCAB).

3.2.1 Degradation-Aware Self-Attention

In CI tasks, the reduction in data dimensionality during the sampling process can lead to inevitable loss of information, resulting in image quality degradation characterized by blurring, noise, and distortion. To address this challenge, we introduce a Degradation-Aware Mask (DAM) into self-attention mechanism, proposing Degradation-Aware Self-Attention (DA-SA), as shown in Fig. 2e and Fig. 2d. The DAM incorporates two domains of degradation perception: the image-level domain and the measurement-level domain. Specifically, given $\overline{\mathbf{x}}^{(k)}$ as the input of the DAM in k-th iteration stage, $\overline{\mathbf{x}}^{(k)}$ undergoes a DCAB and a 1×1 convolution to reduce the channel count to C_0, yielding the current estimated image $\overline{\mathbf{x}}_0^{(k)}$. On one hand, we quantify the image-level degradation $\mathbf{d}_1^{(k)}$, resulting from reduced-dimensional sampling in CI as follows:

$$\mathbf{d}_1^{(k)} = \overline{\mathbf{x}}_0^{(k)} - \widetilde{\mathcal{F}}_{\mathbf{A}}(\mathcal{F}_{\mathbf{A}}(\overline{\mathbf{x}}_0^{(k)})). \tag{4}$$

On the other hand, we obtain the degradation $\mathbf{d}_2^{(k)}$ in the measurement-level domain by subtracting the initial measurement $\mathbf{y}$ from the measurement of $\overline{\mathbf{x}}_0^{(k)}$, which serves as a data fidelity term to maintain consistency between the measurement of current estimated image and the original measurement:

$$\mathbf{d}_2^{(k)} = \widetilde{\mathcal{F}}_{\mathbf{A}}(\mathbf{y} - \mathcal{F}_{\mathbf{A}}(\overline{\mathbf{x}}_0^{(k)})). \tag{5}$$

Subsequently, we concatenate the $\mathbf{d}_1^{(k)}$ and $\mathbf{d}_2^{(k)}$ along the channel dimension, and use a 1×1 convolution and DCAB to increase the channel count, which is succeeded by a Sigmoid function to obtain degradation weights for the degraded regions of the images. We then perform a Hadamard product between $\overline{\mathbf{x}}^{(k)}$ and the obtained degradation weights, followed by a residual connection to obtain the output of the DAM, denoted as $\mathbf{d}^{(k)}$. $\mathbf{d}^{(k)}$ then undergoes a 1×1 convolution to further increase the channel count to $C_h \times N_h$, where C_h denotes the number of channels per head and N_h represents the number of heads. Subsequently, the obtained features are combined with Value $\mathbf{V}$ in DA-SA using a Hadamard product to prioritize attention to the degraded parts and details in the images. The integration of DAM enhances the DUMoE's ability to perceive degraded details, consequently improving feature extraction capabilities and resulting in more representative features.

3.2.2 Multi-Scale Gate

It is crucial to effectively utilize multi-scale features for recovering fine image details (Mou et al. (2022); Cai et al. (2022b)) in CI tasks. Hence, we introduce a U-Block within the gating module and utilize features at different scales to compute gate scores for expert selection. The structure of Multi-Scale Gate (MSGate) is shown in Fig. 2c. Specifically, we employ a 2×2 convolution with

stride of 2 to halve the scale of $\widetilde{\mathbf{x}}^{(k)}$ and double the number of channels. After applying residual connections at the same scale, we utilize a 2×2 transpose convolution to increase the image scale and reduce the number of channels, resulting in three different scales of $\mathbf{x}^{(k)}$, $\mathbf{x}_1^{(k+1)}$, and $\mathbf{x}_2^{(k+1)}$, which are then individually passed through Adaptive Average Pooling (AAP) and concatenated along the channel dimension before being inputted into the Gate. The Gate consists of two linear layers with GELU activation in between, followed by a Softmax operation to obtain corresponding gate scores $w^{(k)} = \{w_1^{(k)}, w_2^{(k)}, w_3^{(k)}\}$. Furthermore, instead of utilizing all three experts, we adopt the top-1 switch routing introduced by Fedus et al. (2022) to sparsify the gating modules and reduce computational overhead. At last, the output is obtained by multiplying the gate score of the corresponding expert with the output of that expert.

3.2.3 DEEP UNFOLDING SPARSA EXPERTS

The detailed structure of Deep Unfolding SpaRSA Experts (DUSE) is presented in Fig. 2b. Specifically, we define $f(\mathbf{x}) = \frac{1}{2}\|\mathbf{A}\mathbf{x} - \mathbf{y}\|_{\ell_2}^2$, and we can transfer Eq. (1) into following iterative steps:

$$\mathbf{x}^{(k+1)} \in \arg\min_{\mathbf{z}} (\mathbf{z} - \mathbf{x}^{(k)})\nabla f(\mathbf{x}^{(k)}) + \frac{\lambda^{(k)}}{2}\|\mathbf{z} - \mathbf{x}^{(k)}\|_{\ell_2}^2 + \tau^{(k)}\mathcal{R}(\mathbf{z}), \tag{6}$$

where $\lambda^{(k)}$ is the penalty term, and $\lambda^{(k)}$ and $\tau^{(k)}$ are learnable parameters independent for each stage. Then we merge the first two terms in Eq. (6) and reformulate it into following two subproblems:

$$\mathbf{u}^{(k)} = \mathbf{x}^{(k)} - \frac{1}{\lambda^{(k)}}\nabla f(\mathbf{x}^{(k)}), \tag{7}$$

$$\mathbf{x}^{(k+1)} \in \arg\min_{\mathbf{z}} \frac{1}{2}\|\mathbf{z} - \mathbf{u}^{(k)}\|_{\ell_2}^2 + \frac{\tau^{(k)}}{\lambda^{(k)}}\mathcal{R}(\mathbf{z}). \tag{8}$$

Specifically, Eq. (7) represents a gradient descent term:

$$\mathbf{u}^{(k)} = \mathbf{x}^{(k)} - \frac{1}{\lambda^{(k)}}\mathbf{A}^\top(\mathbf{A}\mathbf{x}^{(k)} - \mathbf{y}), \tag{9}$$

while Eq. (8) can be viewed as a denoising problem solvable using the proximal mapping operator. Here, we employ ℓ_1-norm as the prior term to induce sparsity in the transformation domain, i.e., $\mathcal{R}(\mathbf{z}) = \|\mathbf{\Psi}\mathbf{z}\|_{\ell_1}$, where $\mathbf{\Psi} \in \mathbb{R}^{N\times N}$ denotes an orthonormal sparse basis. Thus, Eq. (8) can be reformulated as:

$$\mathbf{x}^{(k+1)} \in \arg\min_{\mathbf{z}} \frac{1}{2}\|\mathbf{z} - \mathbf{u}^{(k)}\|_{\ell_2}^2 + \frac{\tau^{(k)}}{\lambda^{(k)}}\|\mathbf{\Psi}\mathbf{z}\|_{\ell_1}. \tag{10}$$

Theorem 1. *Let $\mathbf{z} \in \mathbb{R}^N$, and let $\mathbf{\Psi} \in \mathbb{R}^{N\times N}$ be an orthonormal matrix, i.e., $\mathbf{\Psi}^T\mathbf{\Psi} = \mathbf{I}$, where $\mathbf{I}$ denotes the identity matrix. Then, Parseval's Theorem states that the Euclidean norm of $\mathbf{z}$ is equivalent to the Euclidean norm of its transform $\mathbf{\Psi}\mathbf{z}$, which can be mathematically expressed as:*

$$\|\mathbf{z}\|_{\ell_2}^2 = \mathbf{z}^T\mathbf{z} = (\mathbf{\Psi}\mathbf{z})^T(\mathbf{\Psi}\mathbf{z}) = \|\mathbf{\Psi}\mathbf{z}\|_{\ell_2}^2. \tag{11}$$

According to Theorem 1, the following can be derived:

$$\frac{1}{2}\|\mathbf{z} - \mathbf{u}^{(k)}\|_{\ell_2}^2 = \frac{1}{2}\|\mathbf{\Psi}(\mathbf{z} - \mathbf{u}^{(k)})\|_{\ell_2}^2 = \frac{1}{2}\|\mathbf{\Psi}\mathbf{z} - \mathbf{\Psi}\mathbf{u}^{(k)}\|_{\ell_2}^2. \tag{12}$$

By substituting Eq. (12) into Eq. (10), we arrive at the following expression:

$$\mathbf{x}^{(k+1)} \in \arg\min_{\mathbf{z}} \frac{1}{2}\|\mathbf{\Psi}\mathbf{z} - \mathbf{\Psi}\mathbf{u}^{(k)}\|_{\ell_2}^2 + \frac{\tau^{(k)}}{\lambda^{(k)}}\|\mathbf{\Psi}\mathbf{z}\|_{\ell_1}. \tag{13}$$

By differentiating Eq. (13) and setting the derivative equal to zero, we obtain:

$$(\mathbf{\Psi}\mathbf{z} - \mathbf{\Psi}\mathbf{u}^{(k)}) + \frac{\tau^{(k)}}{\lambda^{(k)}}\mathrm{sgn}(\mathbf{\Psi}\mathbf{z}) = 0. \tag{14}$$

Thus, it follows that:

$$\mathbf{\Psi}\mathbf{z} = \mathrm{soft}(\mathbf{\Psi}\mathbf{u}^{(k)}, \frac{\tau^{(k)}}{\lambda^{(k)}}), \tag{15}$$

Table 1: Average PSNR (dB) (upper) and SSIM (lower) performance comparisons of DUMoE and other ICS methods on various datasets at different sampling ratios (0.01, 0.04, 0.10 and 0.25).

Methods	Urban100					General100					Set14					McM18				
	0.01	0.04	0.10	0.25	Avg.	0.01	0.04	0.10	0.25	Avg.	0.01	0.04	0.10	0.25	Avg.	0.01	0.04	0.10	0.25	Avg.
ISTA-Net$^+$ (CVPR 2018)	16.67 0.3734	19.66 0.5370	23.51 0.7201	28.91 0.8834	22.19 0.6285	17.45 0.4131	21.56 0.624	26.49 0.8036	32.44 0.9237	24.49 0.6911	18.22 0.4014	22.08 0.5708	26.00 0.7289	30.62 0.8700	24.23 0.6428	19.99 0.4942	24.27 0.6577	28.54 0.8104	33.99 0.9237	26.70 0.7215
AMP-Net (TIP 2021)	19.62 0.5025	22.81 0.6825	26.04 0.8151	30.89 0.9202	24.84 0.7301	22.71 0.6282	26.96 0.7695	30.82 0.8722	36.01 0.9508	29.13 0.8052	21.64 0.5433	25.50 0.7007	28.77 0.8183	33.21 0.9144	27.28 0.7442	23.78 0.6426	27.90 0.7879	31.68 0.8860	36.88 0.9560	30.06 0.8181
CASNet (TIP 2022)	20.08 0.5366	23.73 0.7412	27.40 0.8606	32.19 0.9396	25.85 0.7695	23.48 0.6480	28.50 0.8171	32.78 0.9099	38.07 0.9657	30.71 0.8352	22.03 0.5600	26.04 0.7330	29.37 0.8467	33.95 0.9308	27.85 0.7676	24.23 0.6538	28.48 0.8166	32.47 0.9100	37.77 0.9659	30.74 0.8366
DGUNet$^+$ (CVPR 2022)	20.15 0.5335	24.05 0.7478	28.01 0.8709	32.77 0.9452	26.25 0.7744	22.86 0.6190	27.92 0.8078	32.41 0.9073	37.55 0.9645	30.18 0.8247	21.86 0.5409	25.88 0.7250	29.34 0.8455	33.70 0.9294	27.69 0.7602	23.05 0.6267	28.16 0.8091	32.32 0.9070	37.74 0.9655	30.32 0.8271
FSOINet (ICASSP 2022)	19.87 0.5223	23.69 0.7376	27.53 0.8627	32.62 0.9430	25.93 0.7664	23.27 0.6363	28.39 0.8135	32.70 0.9085	38.13 0.9660	30.62 0.8311	22.00 0.5538	26.08 0.7324	29.35 0.8451	34.05 0.9309	27.87 0.7656	24.10 0.6464	28.50 0.8157	32.47 0.9097	37.85 0.9663	30.73 0.8345
TransCS (TIP 2022)	18.98 0.4398	23.27 0.7117	26.77 0.8418	31.77 0.9332	25.20 0.7316	21.66 0.5415	27.25 0.7843	31.39 0.8918	37.08 0.9604	29.34 0.7945	20.91 0.4853	25.50 0.7133	28.81 0.8343	33.37 0.9244	27.15 0.7393	22.81 0.5736	27.94 0.7976	31.88 0.8998	37.27 0.9627	29.98 0.8084
AutoBCS (TCYB 2023)	19.23 0.4991	22.50 0.7029	25.36 0.8242	29.60 0.9187	24.17 0.7362	22.24 0.6164	27.10 0.7964	30.76 0.8927	35.92 0.9581	29.00 0.8159	20.93 0.5343	25.07 0.7153	28.00 0.8286	32.14 0.9203	26.53 0.7496	23.26 0.6248	27.54 0.8002	31.13 0.8973	36.25 0.9608	29.55 0.8208
SODAS-Net (TIM 2023)	17.13 0.3947	20.85 0.5874	26.23 0.8084	31.86 0.9257	24.02 0.6791	19.52 0.5093	24.99 0.6998	30.58 0.8602	36.06 0.9454	27.79 0.7537	18.79 0.4349	23.19 0.6139	27.54 0.7812	32.39 0.8977	25.48 0.6819	20.84 0.5340	25.41 0.7079	30.16 0.8583	35.55 0.9434	27.99 0.7609
TCS-Net (TCI 2023)	19.61 0.4945	22.93 0.7036	25.87 0.8291	30.13 0.9241	24.64 0.7378	22.58 0.5978	26.57 0.7712	29.90 0.8748	34.63 0.9504	28.42 0.7986	21.64 0.5219	25.25 0.7073	28.19 0.8283	32.23 0.9206	26.83 0.7445	23.63 0.6144	27.54 0.7907	30.97 0.8913	35.89 0.9579	29.51 0.8136
CSformer (TIP 2023)	20.14 0.5298	24.03 0.7377	27.30 0.8483	31.83 0.9347	25.83 0.7626	23.35 0.6394	27.81 0.7986	31.60 0.8880	36.51 0.9558	29.82 0.8205	22.07 0.5493	25.87 0.7160	28.79 0.8214	32.95 0.9174	27.42 0.7510	23.66 0.6526	28.12 0.8030	31.69 0.8907	36.60 0.9570	30.02 0.8258
OCTUF (CVPR 2023)	19.88 0.5167	23.68 0.7328	27.79 0.8621	32.99 0.9445	26.08 0.7640	23.31 0.6346	28.35 0.8122	32.77 0.9084	38.26 0.9666	30.67 0.8305	21.94 0.5500	26.04 0.7302	29.47 0.8454	34.18 0.9312	27.91 0.7642	23.87 0.6409	28.33 0.8120	32.49 0.9093	37.93 0.9667	30.66 0.8322
DPC-DUN (TIP 2023)	17.31 0.4216	22.36 0.6768	26.96 0.8361	32.36 0.9323	24.75 0.7167	19.95 0.5363	26.61 0.7531	31.17 0.8716	36.50 0.9481	28.56 0.7773	19.04 0.4551	24.32 0.6630	28.03 0.7950	32.78 0.9023	26.04 0.7038	21.10 0.5553	26.51 0.7539	30.67 0.8701	35.86 0.9462	28.54 0.7814
MTC-CSNet (TCYB 2024)	19.63 0.4906	22.66 0.6858	25.81 0.8284	30.15 0.9228	24.56 0.7319	22.96 0.6122	27.26 0.7843	31.33 0.8970	36.33 0.9596	29.47 0.8133	21.68 0.5295	25.19 0.7018	28.47 0.8333	32.64 0.9226	27.00 0.7468	23.71 0.6227	27.62 0.7884	31.50 0.8999	36.68 0.9623	29.88 0.8183
NesTD-Net (TIP 2024)	20.13 0.5288	23.94 0.7432	27.80 0.8681	33.02 0.9448	26.22 0.7712	23.14 0.6165	28.58 0.8211	32.85 0.9123	38.42 0.9670	30.74 0.8292	22.32 0.5600	26.31 0.7393	29.62 0.8504	34.33 0.9330	28.15 0.7707	24.41 0.6535	28.70 0.8218	32.73 0.9125	37.98 0.9664	30.96 0.8385
LTwIST (TCSVT 2024)	19.46 0.4886	23.01 0.7061	26.76 0.8463	31.79 0.9349	25.26 0.7440	22.69 0.5989	27.53 0.7935	31.91 0.8990	37.31 0.9616	29.86 0.8133	21.49 0.5190	25.47 0.7112	28.88 0.8352	33.42 0.9249	27.31 0.7476	23.44 0.6108	27.64 0.7918	31.73 0.8995	36.97 0.9611	29.95 0.8158
UFC-Net (CVPR 2024)	19.69 0.5041	23.37 0.7195	27.55 0.8583	32.82 0.9423	25.86 0.7561	23.08 0.6145	27.92 0.7988	32.31 0.9014	37.75 0.9624	30.27 0.8193	21.79 0.5324	25.67 0.7163	29.10 0.8363	33.81 0.9259	27.59 0.7527	23.73 0.6240	27.95 0.7984	31.97 0.9011	37.24 0.9619	30.22 0.8214
DUMoE (Our Method)	**20.33** **0.5420**	**24.48** **0.7614**	**28.43** **0.8773**	**33.42** **0.9481**	**26.67** **0.7822**	**24.02** **0.6545**	**28.96** **0.8261**	**33.15** **0.9149**	**38.45** **0.9676**	**31.15** **0.8408**	**22.40** **0.5643**	**26.44** **0.7407**	**29.83** **0.8516**	**34.42** **0.9334**	**28.27** **0.7725**	**24.42** **0.6562**	**28.85** **0.8245**	**32.90** **0.9146**	**38.09** **0.9676**	**31.07** **0.8407**

where soft denotes the soft thresholding function, defined as $\text{soft}(\mathbf{x}, \theta) \equiv \text{sgn}(\mathbf{x}) \max\{|\mathbf{x}| - \theta, 0\}$. Consequently, the closed-form solution of Eq. (13) is given by:

$$\mathbf{x}^{(k+1)} = \mathbf{\Psi}^T \text{soft}(\mathbf{\Psi}\mathbf{u}^{(k)}, \frac{\tau^{(k)}}{\lambda^{(k)}}). \tag{16}$$

However, obtaining $\mathbf{x}^{(k+1)}$ in Eq. (10) remains challenging when $\mathbf{\Psi}$ is non-orthogonal or represents a nonlinear transform (Zhang & Ghanem (2018)). To address this, we substitute $\mathbf{\Psi}$ with a learnable, deep learning-based structure $\mathcal{D}$, as presented in Eq. (17), which allows for learning a sparse representation of $\mathbf{z}$, enhancing both model flexibility and adaptability.

$$\mathbf{x}^{(k+1)} = \widetilde{\mathcal{D}}(\text{soft}(\mathcal{D}(\mathbf{u}^{(k)}), \frac{\tau^{(k)}}{\lambda^{(k)}})), \tag{17}$$

where $\widetilde{\mathcal{D}}$ denotes the left inverse of $\mathcal{D}$. Here, both $\mathcal{D}$ and $\widetilde{\mathcal{D}}$ are depth-wise convolutions with a 3×3 kernel. It is worth noting that the image-level feature transmission in DUNs often results in information loss (Zhang et al. (2022); Song et al. (2023c)) during the reconstruction. Therefore, we use the Sigmoid function and residual connections to achieve the weighted feature fusion and obtain the output of the DUSE, denoted as $\widetilde{\mathbf{x}}^{(k+1)}$, in the k-th iteration stage.

3.3 Loss Function

We adopt different loss functions, denoted as $\mathcal{L}_{\text{deviation}}$, to quantify the deviation between the reconstructed image and the corresponding ground truth image for various CI tasks. For instance, we utilize the ℓ_2-norm loss for ICS and CS-MRI tasks, and the Charbonnier loss (Charbonnier et al. (1994)) for SCI tasks. Furthermore, to promote load balance and competition across different DUSE (Fedus et al. (2022)), we employ the coefficient of variation to measure the dispersion of gate scores of DUSE in each iteration stage:

$$\mathcal{L}_{C_v} = \frac{1}{n} \sum_{k=1}^{n} \left(\frac{\text{std}(w^{(k)})}{\text{mean}(w^{(k)})} \right)^2, \tag{18}$$

where n denotes the number of iteration stages and $w^{(k)} = \{w_1^{(k)}, w_2^{(k)}, w_3^{(k)}\}$ represents the gate scores in the k-th iteration stage. Consequently, the loss function of DUMoE is formulated as follows:

$$\mathcal{L}_{\text{total}} = \mathcal{L}_{\text{deviation}} + \eta \mathcal{L}_{C_v}, \tag{19}$$

where η is the weight of $\mathcal{L}_{C_v}$. In our experiments, we set η to 1×10^{-3}.

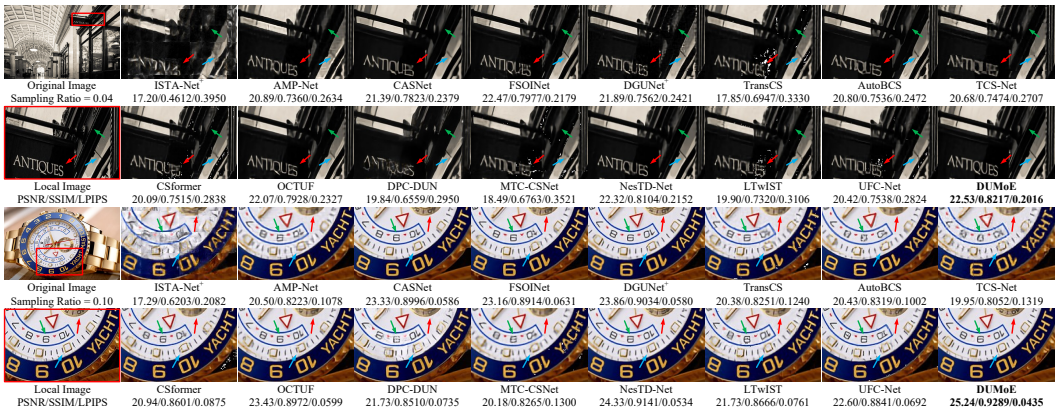

Figure 3: Comparisons of visual results and corresponding PSNR (dB)/SSIM/LPIPS (Zhang et al. (2018)) performance between DUMoE and other advanced ICS methods at sampling ratios of 0.04 and 0.10. Key details are highlighted with arrows. Please zoom in for better comparisons.

4 Experiments

In this section, we conduct extensive experiments across three CI tasks: ICS, CS-MRI, and SCI. We set the default number of iteration stages to $n = 5$ and corresponding channels to $C_1 = 32$, $C_2 = 48$, and $C_3 = 80$. Besides, we highlight the best and second-best results in the tables using red and blue colors, respectively. Further implementation details for each CI task are provided in Appendix A.4. Additionally, more experiments as well as supplementary visualizations are available in Appendix A.5.

4.1 Natural Image Compressive Sensing

We conduct qualitative comparisons between DUMoE and sixteen ICS methods, including ISTA-Net$^+$ (Zhang & Ghanem (2018)), AMP-Net (Zhang et al. (2021)), CASNet (Chen & Zhang (2022)), DGUNet$^+$ (Mou et al. (2022)), FSOINet (Chen et al. (2022)), TransCS (Shen et al. (2022)), AutoBCS (Gan et al. (2023a)), SODAS-Net (Song & Zhang (2023)), TCS-Net (Gan et al. (2023b)), CSformer (Ye et al. (2023)), OCTUF (Song et al. (2023c)), DPC-DUN (Song et al. (2023b)), MTC-CSNet (Shen et al. (2024)), NesTD-Net (Gan et al. (2024a)), LTwIST (Gan et al. (2024b)), and UFC-Net (Wang & Gan (2024)), across four widely-used benchmark datasets: Urban100 (Huang et al. (2015)), General100 (Dong et al. (2016)), Set14 (Zeyde et al. (2012)), and McM18 (Zhang et al. (2011)).

Tab. 1 demonstrates that DUMoE consistently outperforms other methods in terms of PSNR and SSIM across all tested datasets and various sampling ratios. Specifically, on the Urban100 at a sampling ratio of 0.10, DUMoE surpasses OCTUF, LTwIST, DPC-DUN, MTC-CSNet, NesTD-Net and UFC-Net by approximately 0.64 dB (2.30%), 1.67 dB (6.24%), 1.47 dB (5.45%), 2.62 dB (10.15%), 0.63 dB (2.27%), and 0.88 dB (3.19%) in terms of PSNR, respectively. Similarly, regarding SSIM, DUMoE leads by around 0.0152 (1.76%), 0.0310 (3.66%), 0.0412 (4.93%), 0.0489 (5.90%), 0.0092 (1.06%), and 0.0190 (2.21%), respectively. Moreover, Fig. 3 shows that DUMoE consistently achieves superior performance in terms of human perception quality compared to methods such as NesTD-Net, LTwIST, UFC-Net, and others. Even at low sampling ratios of 0.04 and 0.10, DUMoE excels in recovering fine-grained image details with reduced noise, distortion, blurring, and absence of blocking artifacts. This underscores the effectiveness of DUMoE in reconstructing images with higher human perception quality and overall image quality. For additional experiments at high sampling ratios, please refer to Appendix A.5.1.

4.2 Compressive Sensing MRI

As shown in Tab. 2, we compare DUMoE with eleven CS-MRI methods, including ISTA-Net$^+$ (Zhang & Ghanem (2018)), RDN (Sun et al. (2018)), DC-CNN (Schlemper et al. (2018)), CDDN (Zheng et al. (2019)), ADMM-CSNet (Yang et al. (2020)), NESTANets (Neyra-Nesterenko & Adcock (2022)),

Table 2: Average PSNR (dB) and SSIM performance comparisons of DUMoE and other CS-MRI methods on Brain dataset at various sampling ratios (0.05, 0.10, 0.20, 0.30 and 0.40).

Methods	0.05		0.10		0.20		0.30		0.40		Avg.	
	PSNR	SSIM	PSNR	SSIM	PSNR	SSIM	PSNR	SSIM	PSNR	SSIM	PSNR	SSIM
Zero-filled	24.20	0.5417	26.81	0.6030	30.41	0.7229	33.01	0.8023	35.14	0.8568	29.91	0.7053
ISTA-Net$^+$ (CVPR 2018)	31.28	0.8547	34.62	0.9035	38.57	0.9478	40.90	0.9631	42.62	0.9724	37.60	0.9283
RDN (AAAI 2018)	30.95	0.8421	34.38	0.8998	38.47	0.9474	40.82	0.9630	42.50	0.9719	37.42	0.9248
DC-CNN (TMI 2018)	30.81	0.8370	34.33	0.8957	38.43	0.9467	40.53	0.9526	42.02	0.9717	37.22	0.9207
CDDN (NeurIPS 2019)	31.58	0.8513	34.67	0.9014	38.65	0.9476	40.95	0.9633	42.74	0.9731	37.72	0.9273
ADMM-CSNet (TPAMI 2020)	31.37	0.8608	34.45	0.8985	38.52	0.9471	40.81	0.9629	42.71	0.9729	37.57	0.9284
NESTANets (STSPDA 2022)	26.65	0.6044	30.79	0.7670	35.20	0.8866	38.07	0.9314	40.16	0.9523	34.17	0.8283
HiTDUN (J-STSP 2022)	32.72	0.8770	35.35	0.9104	39.02	0.9510	41.21	0.9651	42.87	0.9737	38.23	0.9354
PUERT (J-STSP 2022)	31.51	0.8542	34.84	0.9068	38.78	0.9495	41.01	0.9642	42.73	0.9732	37.77	0.9296
LTwIST (TCSVT 2024)	31.30	0.8536	34.11	0.9043	36.68	0.9361	39.46	0.9523	41.47	0.9663	36.60	0.9225
NesTD-Net (TIP 2024)	33.71	0.8934	36.15	0.9243	39.43	0.9536	41.32	0.9658	42.90	0.9740	38.70	0.9422
UFC-Net (CVPR 2024)	32.63	0.8779	34.68	0.9064	38.85	0.9502	41.04	0.9644	42.73	0.9732	37.99	0.9344
DUMoE (Our Method)	**34.28**	**0.9047**	**36.39**	**0.9274**	**39.65**	**0.9555**	**41.57**	**0.9668**	**43.11**	**0.9746**	**39.00**	**0.9458**

Table 3: PSNR (dB)/SSIM performance comparisons of DUMoE and other SCI methods on 10 simulation scenes.

Methods	Scene1	Scene2	Scene3	Scene4	Scene5	Scene6	Scene7	Scene8	Scene9	Scene10	Avg.
GAP-TV (ICIP 2017)	28.16/0.913	23.90/0.818	20.44/0.762	23.33/0.872	28.11/0.920	27.69/0.885	20.62/0.811	24.68/0.831	22.84/0.800	23.02/0.843	24.28/0.845
DeSCI (TPAMI 2019)	28.30/0.910	27.46/0.901	31.98/0.955	32.56/0.971	28.06/0.933	27.43/0.914	25.51/0.945	24.51/0.876	31.80/0.935	22.29/0.822	27.99/0.916
Lambda-Net (ICCV 2019)	29.71/0.830	27.70/0.742	29.53/0.846	37.53/0.911	26.60/0.790	27.25/0.787	26.61/0.782	26.20/0.781	28.54/0.798	26.14/0.701	28.58/0.797
ADMM-Net (ICCV 2019)	34.09/0.924	33.58/0.904	35.02/0.935	41.24/0.972	31.79/0.926	32.52/0.929	32.38/0.901	30.68/0.912	33.70/0.921	30.64/0.905	33.56/0.923
TSA-Net (ECCV 2020)	32.31/0.898	31.07/0.863	32.30/0.918	39.53/0.959	29.44/0.887	31.06/0.905	30.26/0.883	29.31/0.893	31.62/0.912	29.20/0.867	31.61/0.899
DGSMP (CVPR 2021)	33.35/0.920	31.66/0.892	32.93/0.925	40.39/0.970	29.46/0.894	32.74/0.938	31.14/0.898	31.32/0.932	31.53/0.925	31.51/0.934	32.60/0.923
MST-L (CVPR 2022)	35.43/0.946	36.11/0.949	36.39/0.955	42.05/0.977	32.94/0.950	34.71/0.957	34.08/0.932	32.88/0.953	35.04/0.947	32.74/0.946	35.24/0.951
HDNet (CVPR 2022)	35.10/0.940	35.65/0.943	36.04/0.948	42.47/0.978	32.67/0.950	34.46/0.956	33.64/0.930	32.43/0.948	34.86/0.947	32.34/0.943	34.97/0.948
CST-L+ (ECCV 2022)	35.87/0.954	36.84/0.958	38.20/0.966	42.53/0.982	33.11/0.958	35.76/0.967	34.73/0.947	34.33/0.967	36.31/0.961	33.04/0.952	36.07/0.961
BiSRNet (NeurIPS 2023)	30.87/0.853	29.22/0.795	28.97/0.830	35.87/0.909	28.20/0.828	30.19/0.860	27.81/0.806	28.71/0.845	29.39/0.834	27.84/0.810	29.71/0.837
RDFNet (TCI 2023)	33.40/0.950	32.38/0.954	34.47/0.961	37.70/0.976	32.67/0.957	35.80/0.963	27.67/0.939	33.09/0.956	34.66/0.958	31.54/0.949	33.34/0.956
GAP-Net (IJCV 2023)	33.62/0.926	30.08/0.914	33.07/0.944	40.94/0.966	30.77/0.925	33.60/0.936	27.41/0.915	31.25/0.918	33.56/0.937	30.36/0.914	32.47/0.929
EDUNet (NN 2024)	36.48/0.951	37.65/0.961	37.19/0.963	42.85/0.981	34.29/0.962	35.70/0.966	35.37/0.949	34.18/0.962	36.81/0.960	33.46/0.951	36.40/0.961
DWMT (AAAI 2024)	36.46/0.957	37.75/0.963	38.47/0.965	44.23/0.984	33.99/0.963	36.17/0.970	35.22/0.949	34.56/0.968	37.41/0.965	34.00/0.959	36.83/0.964
DUMoE (Our Method)	**36.73/0.959**	**38.87/0.971**	**40.46/0.974**	**45.69/0.989**	**34.87/0.969**	**36.58/0.973**	**35.88/0.952**	**34.78/0.971**	**38.79/0.971**	**33.74/0.959**	**37.64/0.969**

HiTDUN (Zhang et al. (2022)), PUERT (Xie et al. (2022)), NesTD-Net (Gan et al. (2024a)), LTwIST (Gan et al. (2024b)), and UFC-Net (Wang & Gan (2024)) on the widely-used Brain dataset (Yang et al. (2020)) using Pseudo Radial masks as sub-sampling matrix. Specifically, at a sampling ratio of 0.05, DUMoE significantly outperforms NesTD-Net, LTwIST, and UFC-Net, with improvements of approximately 0.57 dB (1.69%), 2.98 dB (9.52%), and 1.65 dB (5.06%) in PSNR, respectively, and leads by around 0.0113 (1.26%), 0.0511 (5.99%), and 0.0268 (3.05%) in terms of SSIM, respectively. For additional visualizations, please refer to Appendix A.5.2.

4.3 Snapshot Compressive Imaging

We perform qualitative comparisons between DUMoE and fourteen SCI methods, namely GAP-TV (Yuan (2016)), DeSCI (Liu et al. (2019)) Lambda-Net (Miao et al. (2019)), ADMM-Net (Ma et al. (2019)), TSA-Net (Meng et al. (2020)), DGSMP (Huang et al. (2021)), MST-L (Cai et al. (2022b)), HDNet (Hu et al. (2022)), CST-L$^+$ (Cai et al. (2022a)), BiSRNet (Cai et al. (2023)), RDFNet (Zhou et al. (2023)), GAP-Net (Meng et al. (2023)), EDUNet (Qin et al. (2024)) and DWMT (Luo et al. (2024)), using widely-used ten scenes from KAIST dataset (Choi et al. (2017)). As shown in Tab. 3, when compared to GAP-Net, RDFNet, EDUNet, and DWMT, DUMoE achieves an average PSNR improvement of approximately 5.17 dB (15.92%), 4.30 dB (12.90%), 1.24 dB (3.41%), and 0.81 dB (2.20%) across the ten scenes, respectively. Moreover, in terms of average SSIM on ten scenes, DUMoE maintains a lead of approximately 0.040 (4.31%), 0.013 (1.36%), 0.008 (0.83%), and 0.005 (0.52%), respectively. For additional visualizations and experiments on real HSI data, please refer to Appendix A.5.3.

5 Discussion

In this section, we delve into several discussions concerning DUMoE, primarily based on ICS experiments, but the insights are equally applicable to other tasks as well.

Table 4: Ablation studies on different cases (a) and number of iteration stages (b), as well as complexity analysis of various methods (c).

(a) PSNR (dB), SSIM, parameters (M) and FLOPs (G) for different ablation cases on various datasets at a sampling ratio of 0.25.

Cases	Urban100		General100		Set14		McM18		Params.	FLOPs
	PSNR	SSIM	PSNR	SSIM	PSNR	SSIM	PSNR	SSIM		
w/o SR	33.39	0.9479	38.41	0.9675	34.39	0.9329	38.12	0.9675	4.17	158.72
w/o DUSE	33.30	0.9469	38.34	0.9674	34.35	0.9333	38.03	0.9675	4.43	150.53
w/o MSGate	31.15	0.9289	37.34	0.9629	33.24	0.9252	37.39	0.9642	1.18	92.77
w/o DAM	33.21	0.9465	38.30	0.9672	34.29	0.9325	38.02	0.9670	3.92	116.74
DUMoE	33.42	0.9481	38.45	0.9676	34.42	0.9334	38.09	0.9676	4.17	142.34

(b) PSNR (dB)/SSIM, parameters (M) and FLOPs (G) for different number of stages in DUMoE on General100 at a sampling ratio of 0.10.

Stages	3	4	5 (default)	7	5 (w/o share weights)
PSNR/SSIM	32.88/0.9128	33.00/0.9132	33.15/0.9149	33.24/0.9151	32.98/0.9139
Params.	4.01	4.01	4.01	4.01	5.87
FLOPs	91.18	117.76	141.31	190.46	141.31

(c) Comparisons of various resources required by different methods on a 256×256 image at a sampling ratio of 0.10.

Methods	Params. (M)	FLOPs (G)	Inference time (ms)	Inference memory (MB)	Model size (MB)
CASNet	16.90	205.24	33±2	1652	64.77
DGUNet$^+$	6.81	97.79	27±1	1124	26.61
FSOINet	0.64	17.19	8±2	852	2.53
TransCS	1.49	25.86	187±26	515	20.43
AutoBCS	2.01	20.11	26±3	651	7.72
SODAS-Net	0.92	64.69	10±7	720	3.54
TCS-Net	0.52	7.04	5±3	1553	3.23
OCTUF	0.40	21.51	16±6	824	1.67
DPC-DUN	1.64	65.54	25±5	579	6.43
MTC-CSNet	0.92	20.61	10±0	605	3.61
NesTD-Net	5.57	347.92	82±12	1957	21.38
LTwIST	23.49	110.46	103±6	707	89.99
UFC-Net	1.74	115.58	84±28	844	7.19
DUMoE	4.01	141.31	78±6	1745	15.46

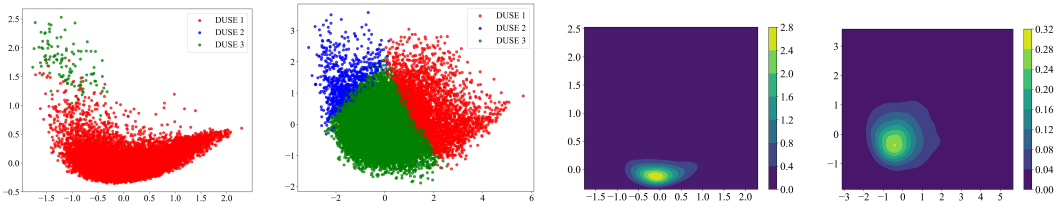

(a) PCA visualization of hidden states in w/o MSGate.

(b) PCA visualization of hidden states in DUMoE.

(c) Gaussian KDE visualization of hidden states in w/o MSGate.

(d) Gaussian KDE visualization of hidden states in DUMoE.

Figure 4: Analysis of the representation collapse of the hidden states in MSGate of DUMoE. (a) and (b) illustrate the spatial structure of the experts using Principal Component Analysis (PCA), where each data point represents an image to be routed, and its color corresponds to the assigned DUSE. (c) and (d) show the diversity of these hidden states, computed using Gaussian Kernel Density Estimation (KDE) and visualized as heatmaps.

5.1 Ablation Study

Different components. We perform ablation experiments to evaluate the contributions of switch routing strategy, DUSE, MSGate, and DAM within the DUMoE architecture. Specifically, we obtain the ablation cases by adopting all the experts instead of switch routing (w/o SR), replacing DUSE with two 3×3 convolutions and GELU activation in between (w/o DUSE), replacing MSGate with a linear layer (w/o MSGate), and removing DAM from DA-SA (w/o DAM).

First, as shown in Tab. 4a, DUMoE achieves better or comparable performance with the same parameter counts and fewer Floating Point Operations (FLOPs) compared to w/o SR, while also achieving superior performance with fewer parameters and FLOPs compared to w/o DUSE, demonstrating the effectiveness of the switch routing strategy and our proposed DUSE.

Furthermore, as illustrated in Fig. 4, we visualize and analyze the hidden states (i.e., the input features of the gate module) in the MSGate of DUMoE from the aspect of representation collapse (Chi et al. (2022)). We employ images from the CIFAR-10 and CIFAR-100 test sets (Krizhevsky (2009)), comprising a total of 20,000 images, for visualizations and analyses.

Initially, we use Principal Component Analysis (PCA) to extract the first two principal components from the hidden states. As illustrated in Fig. 4a and Fig. 4b, each data point represents an image to be routed, with its color corresponding to the assigned DUSE. In Fig. 4a, the points are predominantly mixed together, indicative of unbalanced routing. Conversely, in Fig. 4b, DUMoE exhibits a well-structured feature space with clear cluster distinctions, suggesting successful projection of images by our MSGate while preserving routing features.

Subsequently, we apply Gaussian Kernel-Density Estimation (KDE) to the hidden states processed by PCA, using the Scott method as the bandwidth estimator. Compared to Fig. 4c, Fig. 4d showcases uniformly distributed hidden states, indicating balanced expert assignment and reduced representation collapse (Chi et al. (2022)).

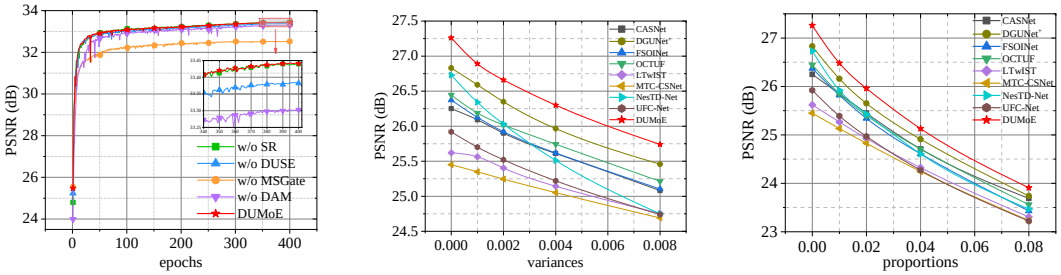

(a) PSNR (dB) of different ablation cases on the validation set at a sampling ratio of 0.25 during the training epochs.

(b) PSNR (dB) of different methods on Set11 at a sampling ratio of 0.04 under different Gaussian noise levels.

(c) PSNR (dB) of different methods on Set11 at a sampling ratio of 0.04 under different pepper-and-salt noise levels.

Figure 5: PSNR (dB) for different ablation cases on validation set during the training epochs (a), different levels of Gaussian noise (b) and pepper-and-salt noise (c) for various methods on Set11.

Finally, as shown in Fig. 5a, compared to other cases, w/o DAM converges more slowly in the initial epochs and does not perform as well as DUMoE in the final convergence. This demonstrates that DAM effectively guides DUMoE to focus on degraded image areas while enhancing attention to crucial details, thus improving feature extraction capabilities. Besides, we provide more visual analyses of the DAM and feature maps at each stage in Appendix A.5.4 and Appendix A.5.5, respectively.

Number of iteration stages. We explore the influence of varying the number of iteration stages in DUMoE, specifically examining configurations with 3, 4, 5 (default), and 7 stages. As presented in Tab. 4b, due to the weight sharing across intermediate stages, DUMoE's performance is observed to scale with FLOPs without increasing the parameter counts, underscoring the effectiveness of our iterative network design. Moreover, compared to the case of w/o sharing weights, DUMoE achieves superior performance with same FLOPs and fewer parameters.

5.2 Complexity Analysis

We conduct a thorough analysis of computational efficiency and hardware utilization for DUMoE and other methods on a 256×256 image with a sampling ratio of 0.10 on the RTX 4090 GPU. Average inference time (ms) and its standard deviation are computed over 500 passes, with memory consumption measured using the nvidia-smi command. Model size reflects the storage requirements of each model, along with reported parameter counts and FLOPs for comparison. As indicated in Tab. 4c, when compared to CASNet, DGUNet$^+$, and NesTD-Net—each achieving several second-best results in Tab. 1—our proposed DUMoE demonstrates superior performance while featuring fewer parameters than CASNet, DGUNet$^+$, and NesTD-Net, as well as fewer FLOPs than CASNet and NesTD-Net. Notably, in comparison to NesTD-Net, DUMoE achieves superior performance while reducing parameters by 1.56 M (28.01%), and FLOPs by 206.61 G (59.38%).

5.3 Performance Under Noise

We assess the robustness of our DUMoE under various levels of Gaussian and pepper-and-salt noise to demonstrate its effectiveness. Specifically, we introduce four levels of Gaussian noise variances (0.001, 0.002, 0.004, and 0.008) and pepper-and-salt proportions (0.01, 0.02, 0.4, and 0.08) to the Set11 (Kulkarni et al. (2016)) and evaluate the model's performance on these noisy images. As shown in Fig. 5b and Fig. 5c, while the performance of each method declines with increasing noise levels, DUMoE consistently outperforms the other methods across all tested noise levels.

6 Conclusion

In this paper, we propose DUMoE, a novel sparse Deep Unfolding MoE framework for CI tasks. DUMoE addresses key challenges in CI recovery problems by integrating innovative components: the DAM, MSGate, and DUSE. Notably, our work represents the first attempt to study deep unfolding paradigm within the MoE framework. Extensive experiments across various CI tasks, including ICS, CS-MRI and SCI, demonstrate the superior performance and effectiveness of our proposed DUMoE.

REFERENCES

Amir Beck and Marc Teboulle. A fast iterative shrinkage-thresholding algorithm for linear inverse problems. *SIAM J. Imaging Sci.*, 2(1):183–202, January 2009. doi: 10.1137/080716542.

JosÉ M. Bioucas-Dias and MÁrio A. T. Figueiredo. A new TwIST: Two-step iterative shrinkage/thresholding algorithms for image restoration. *IEEE Trans. Image Process.*, 16(12):2992–3004, December 2007. ISSN 1941-0042. doi: 10.1109/TIP.2007.909319.

Stephen Boyd. Distributed optimization and statistical learning via the alternating direction method of multipliers. *Found. Trends Mach. Learn.*, 3(1):1–122, 2010. ISSN 1935-8237, 1935-8245. doi: 10.1561/2200000016.

Yuanhao Cai, Jing Lin, Xiaowan Hu, Haoqian Wang, Xin Yuan, Yulun Zhang, Radu Timofte, and Luc Van Gool. Coarse-to-Fine Sparse Transformer for Hyperspectral Image Reconstruction. In Shai Avidan, Gabriel Brostow, Moustapha Cissé, Giovanni Maria Farinella, and Tal Hassner (eds.), *Eur. Conf. Comput. Vis. (ECCV)*, Lecture Notes Comput. Sci., pp. 686–704, 2022a. ISBN 978-3-031-19790-1. doi: 10.1007/978-3-031-19790-1_41.

Yuanhao Cai, Jing Lin, Xiaowan Hu, Haoqian Wang, Xin Yuan, Yulun Zhang, Radu Timofte, and Luc Van Gool. Mask-guided spectral-wise transformer for efficient hyperspectral image reconstruction. In *IEEE/CVF Conf. Comput. Vis. Pattern Recognit. (CVPR)*, pp. 17502–17511, 2022b.

Yuanhao Cai, Jing Lin, Haoqian Wang, Xin Yuan, Henghui Ding, Yulun Zhang, Radu Timofte, and Luc V. Gool. Degradation-aware unfolding half-shuffle transformer for spectral compressive imaging. In *Adv. Neural Inf. Process. Syst. (NeurIPS)*, volume 35, pp. 37749–37761, December 2022c.

Yuanhao Cai, Yuxin Zheng, Jing Lin, Xin Yuan, Yulun Zhang, and Haoqian Wang. Binarized spectral compressive imaging. In A. Oh, T. Naumann, A. Globerson, K. Saenko, M. Hardt, and S. Levine (eds.), *Adv. Neural Inf. Process. Syst. (NeurIPS)*, volume 36, pp. 38335–38346, 2023.

Emmanuel J Candès and Michael B Wakin. An introduction to compressive sampling. *IEEE Signal Process. Mag.*, 25(2):21–30, 2008.

Antonin Chambolle and Thomas Pock. A First-order primal-dual algorithm for convex problems with applications to imaging. *J. Math Imaging Vis.*, 40(1):120–145, May 2011. ISSN 0924-9907, 1573-7683. doi: 10.1007/s10851-010-0251-1.

P. Charbonnier, L. Blanc-Feraud, G. Aubert, and M. Barlaud. Two deterministic half-quadratic regularization algorithms for computed imaging. In *Proc. 1st Int. Conf. Image Process.*, volume 2, pp. 168–172. IEEE Comput. Soc. Press, 1994. ISBN 978-0-8186-6952-1. doi: 10.1109/ICIP.1994.413553.

Bin Chen and Jian Zhang. Content-aware scalable deep compressed sensing. *IEEE Trans. Image Process.*, 31:5412–5426, 2022. ISSN 1941-0042. doi: 10.1109/TIP.2022.3195319.

Bin Chen, Jiechong Song, Jingfen Xie, and Jian Zhang. Deep physics-guided unrolling generalization for compressed sensing. *Int. J. Comput. Vis.*, 131(11):2864–2887, November 2023a. ISSN 1573-1405. doi: 10.1007/s11263-023-01814-w.

Tianlong Chen, Xuxi Chen, Xianzhi Du, Abdullah Rashwan, Fan Yang, Huizhong Chen, Zhangyang Wang, and Yeqing Li. AdaMV-MoE: Adaptive multi-task vision mixture-of-experts. In *Int. Conf. Comput. Vis. (ICCV)*, pp. 17346–17357, 2023b.

Wenjun Chen, Chunling Yang, and Xin Yang. FSOINET: Feature-space optimization-inspired network for image compressive sensing. In *IEEE Int. Conf. Acoust. Speech Signal Process. (ICASSP)*, pp. 2460–2464, May 2022. doi: 10.1109/ICASSP43922.2022.9746648.

Ziheng Cheng, Bo Chen, Ruiying Lu, Zhengjue Wang, Hao Zhang, Ziyi Meng, and Xin Yuan. Recurrent neural networks for snapshot compressive imaging. *IEEE Trans. Pattern Anal. Mach. Intell.*, 45(2):2264–2281, February 2023. ISSN 1939-3539. doi: 10.1109/TPAMI.2022.3161934.

Zewen Chi, Li Dong, Shaohan Huang, Damai Dai, Shuming Ma, Barun Patra, Saksham Singhal, Payal Bajaj, Xia Song, Xian-Ling Mao, Heyan Huang, and Furu Wei. On the representation collapse of sparse mixture of experts. In *Adv. Neural Inf. Process. Syst. (NeurIPS)*, volume 35, pp. 34600–34613, December 2022.

I. Choi, M. H. Kim, D. Gutierrez, D. S. Jeon, and G. Nam. High-quality hyperspectral reconstruction using a spectral prior. In *ACM Trans. Graph.*, number ART-2017-104309, 2017. doi: 10.1145/3130800.3130810.

Chao Dong, Chen Change Loy, and Xiaoou Tang. Accelerating the super-resolution convolutional neural network. In Bastian Leibe, Jiri Matas, Nicu Sebe, and Max Welling (eds.), *Eur. Conf. Comput. Vis. (ECCV)*, pp. 391–407, 2016. ISBN 978-3-319-46475-6. doi: 10.1007/978-3-319-46475-6_25.

Yubo Dong, Dahua Gao, Tian Qiu, Yuyan Li, Minxi Yang, and Guangming Shi. Residual degradation learning unfolding framework with mixing priors across spectral and spatial for compressive spectral imaging. In *IEEE/CVF Conf. Comput. Vis. Pattern Recognit. (CVPR)*, pp. 22262–22271, 2023.

David L. Donoho, Arian Maleki, and Andrea Montanari. Message-passing algorithms for compressed sensing. *Natl. Acad. Sci.*, 106(45):18914–18919, November 2009. doi: 10.1073/pnas.0909892106.

Alexey Dosovitskiy, Lucas Beyer, Alexander Kolesnikov, Dirk Weissenborn, Xiaohua Zhai, Thomas Unterthiner, Mostafa Dehghani, Matthias Minderer, Georg Heigold, Sylvain Gelly, Jakob Uszkoreit, and Neil Houlsby. An image is worth 16x16 words: Transformers for image recognition at scale. In *Int. Conf. Learn. Representations (ICLR)*, June 2021.

Nikoli Dryden and Torsten Hoefler. Spatial mixture-of-experts. In *Adv. Neural Inf. Process. Syst. (NeurIPS)*, volume 35, pp. 11697–11713, December 2022.

William Fedus, Barret Zoph, and Noam Shazeer. Switch Transformers: Scaling to trillion parameter models with simple and efficient sparsity. *J. Mach. Learn. Res.*, 23(1):120:5232–120:5270, January 2022. ISSN 1532-4435.

Hongping Gan, Yang Gao, Chunyi Liu, Haiwei Chen, Tao Zhang, and Feng Liu. AutoBCS: Block-based image compressive sensing with data-driven acquisition and noniterative reconstruction. *IEEE Trans. Cybern.*, 53(4):2558–2571, April 2023a. ISSN 2168-2275. doi: 10.1109/TCYB.2021.3127657.

Hongping Gan, Minghe Shen, Yi Hua, Chunyan Ma, and Tao Zhang. From patch to pixel: A transformer-based hierarchical framework for compressive image sensing. *IEEE Trans. Comput. Imaging*, 9:133–146, 2023b. ISSN 2333-9403. doi: 10.1109/TCI.2023.3244396.

Hongping Gan, Zhen Guo, and Feng Liu. NesTD-Net: Deep NESTA-inspired unfolding network with dual-path deblocking structure for image compressive sensing. *IEEE Trans. Image Process.*, 33:1923–1937, 2024a. ISSN 1941-0042. doi: 10.1109/TIP.2024.3371351.

Hongping Gan, Xiaoyang Wang, Lijun He, and Jie Liu. Learned two-step iterative shrinkage thresholding algorithm for deep compressive sensing. *IEEE Trans. Circuits Syst. Video Technol.*, 34(5):3943–3956, May 2024b. ISSN 1558-2205. doi: 10.1109/TCSVT.2023.3325340.

Tom Goldstein and Stanley Osher. The split bregman method for ℓ_1-regularized problems. *SIAM J. Imaging Sci.*, 2(2):323–343, January 2009. ISSN 1936-4954. doi: 10.1137/080725891.

Elaine T. Hale, Wotao Yin, and Yin Zhang. Fixed-point continuation for ℓ_1-minimization: Methodology and convergence. *SIAM J. Optim.*, 19(3):1107–1130, 2008. doi: 10.1137/070698920.

Xiaowan Hu, Yuanhao Cai, Jing Lin, Haoqian Wang, Xin Yuan, Yulun Zhang, Radu Timofte, and Luc Van Gool. HDNet: High-resolution dual-domain learning for spectral compressive imaging. In *IEEE/CVF Conf. Comput. Vis. Pattern Recognit. (CVPR)*, pp. 17542–17551, 2022.

Jia-Bin Huang, Abhishek Singh, and Narendra Ahuja. Single image super-resolution from transformed self-exemplars. In *IEEE Conf. Comput. Vis. Pattern Recognit. (CVPR)*, pp. 5197–5206, June 2015. ISBN 978-1-4673-6964-0. doi: 10.1109/CVPR.2015.7299156.

Tao Huang, Weisheng Dong, Xin Yuan, Jinjian Wu, and Guangming Shi. Deep Gaussian scale mixture prior for spectral compressive imaging. In *IEEE/CVF Conf. Comput. Vis. Pattern Recognit. (CVPR)*, pp. 16216–16225, 2021.

Alex Krizhevsky. Learning multiple layers of features from tiny images. Technical report, University of Toronto, 2009.

Kuldeep Kulkarni and Pavan Turaga. Reconstruction-free action inference from compressive imagers. *IEEE Trans. Pattern Anal. Mach. Intell.*, 38(4):772–784, 2015.

Kuldeep Kulkarni, Suhas Lohit, Pavan Turaga, Ronan Kerviche, and Amit Ashok. ReconNet: Non-iterative reconstruction of images from compressively sensed measurements. In *IEEE Conf. Comput. Vis. Pattern Recognit. (CVPR)*, pp. 449–458, 2016.

Bo Li, Yifei Shen, Jingkang Yang, Yezhen Wang, Jiawei Ren, Tong Che, Jun Zhang, and Ziwei Liu. Sparse mixture-of-experts are domain generalizable learners. In *Int. Conf. Learn. Representations (ICLR)*, pp. 1–16, 2023a.

Miaoyu Li, Ying Fu, Ji Liu, and Yulun Zhang. Pixel adaptive deep unfolding transformer for hyperspectral image reconstruction. In *IEEE/CVF Int. Conf. Comput. Vis. (ICCV)*, pp. 12959–12968, 2023b.

Tsung-Yi Lin, Michael Maire, Serge Belongie, James Hays, Pietro Perona, Deva Ramanan, Piotr Dollár, and C. Lawrence Zitnick. Microsoft COCO: Common objects in context. In *Eur. Conf. Comput. Vis. (ECCV)*, pp. 740–755, 2014. ISBN 978-3-319-10602-1.

Yang Liu, Xin Yuan, Jinli Suo, David J. Brady, and Qionghai Dai. Rank minimization for snapshot compressive imaging. *IEEE Trans. Pattern Anal. Mach. Intell.*, 41(12):2990–3006, December 2019. ISSN 1939-3539. doi: 10.1109/TPAMI.2018.2873587.

Ilya Loshchilov and Frank Hutter. Decoupled weight decay regularization, January 2019.

Fulin Luo, Xi Chen, Xiuwen Gong, Weiwen Wu, and Tan Guo. Dual-window multiscale transformer for hyperspectral snapshot compressive imaging. *AAAI Conf. Artif. Intell. (AAAI)*, 38(4):3972–3980, March 2024. ISSN 2374-3468. doi: 10.1609/aaai.v38i4.28190.

Michael Lustig, David Donoho, and John M. Pauly. Sparse MRI: The application of compressed sensing for rapid MR imaging. *Magn. Reson. Medicine*, 58(6):1182–1195, 2007. ISSN 1522-2594. doi: 10.1002/mrm.21391.

Michael Lustig, David L. Donoho, Juan M. Santos, and John M. Pauly. Compressed sensing MRI. *IEEE Signal Process. Mag.*, 25(2):72–82, March 2008. ISSN 1558-0792. doi: 10.1109/MSP.2007.914728.

Jiawei Ma, Xiao-Yang Liu, Zheng Shou, and Xin Yuan. Deep tensor admm-net for snapshot compressive imaging. In *IEEE/CVF Int. Conf. Comput. Vis. (ICCV)*, pp. 10223–10232, 2019.

Ziyi Meng, Jiawei Ma, and Xin Yuan. End-to-end low cost compressive spectral imaging with spatial-spectral self-attention. In Andrea Vedaldi, Horst Bischof, Thomas Brox, and Jan-Michael Frahm (eds.), *Eur. Conf. Comput. Vis. (ECCV)*, Lecture Notes Comput. Sci., pp. 187–204, 2020. ISBN 978-3-030-58592-1. doi: 10.1007/978-3-030-58592-1_12.

Ziyi Meng, Xin Yuan, and Shirin Jalali. Deep unfolding for snapshot compressive imaging. *Int. J. Comput. Vis.*, 131(11):2933–2958, November 2023. ISSN 1573-1405. doi: 10.1007/s11263-023-01844-4.

Xin Miao, Xin Yuan, Yunchen Pu, and Vassilis Athitsos. Lambda-Net: Reconstruct hyperspectral images from a snapshot measurement. In *IEEE/CVF Int. Conf. Comput. Vis. (ICCV)*, pp. 4058–4068, October 2019. doi: 10.1109/ICCV.2019.00416.

Chong Mou, Qian Wang, and Jian Zhang. Deep generalized unfolding networks for image restoration. In *IEEE/CVF Conf. Comput. Vis. Pattern Recognit. (CVPR)*, pp. 17378–17389, June 2022. ISBN 978-1-66546-946-3. doi: 10.1109/CVPR52688.2022.01688.

Basil Mustafa, Carlos Riquelme, Joan Puigcerver, Rodolphe Jenatton, and Neil Houlsby. Multimodal contrastive learning with LIMoE: The language-image mixture of experts. In *Adv. Neural Inf. Process. Syst. (NeurIPS)*, volume 35, pp. 9564–9576, December 2022.

Maksym Neyra-Nesterenko and Ben Adcock. NESTANets: Stable, accurate and efficient neural networks for analysis-sparse inverse problems. *Sampl. Theory Signal Process. Data Anal.*, 21(1):4, December 2022. ISSN 2730-5724. doi: 10.1007/s43670-022-00043-5.

Jong-Il Park, Moon-Hyun Lee, Michael D. Grossberg, and Shree K. Nayar. Multispectral imaging using multiplexed illumination. In *IEEE Int. Conf. Comput. Vis. (ICCV)*, pp. 1–8, October 2007. doi: 10.1109/ICCV.2007.4409090.

Adam Paszke, Sam Gross, Francisco Massa, Adam Lerer, James Bradbury, Gregory Chanan, Trevor Killeen, Zeming Lin, Natalia Gimelshein, Luca Antiga, Alban Desmaison, Andreas Kopf, Edward Yang, Zachary DeVito, Martin Raison, Alykhan Tejani, Sasank Chilamkurthy, Benoit Steiner, Lu Fang, Junjie Bai, and Soumith Chintala. PyTorch: An imperative style, high-performance deep learning library. In *Adv. Neural Inf. Process. Syst. (NeurIPS)*, volume 32, 2019.

Joan Puigcerver, Rodolphe Jenatton, Carlos Riquelme, Pranjal Awasthi, and Srinadh Bhojanapalli. On the adversarial robustness of mixture of experts. In *Adv. Neural Inf. Process. Syst. (NeurIPS)*, volume 35, pp. 9660–9671, December 2022.

Xinran Qin, Yuhui Quan, and Hui Ji. Enhanced deep unrolling networks for snapshot compressive hyperspectral imaging. *Neural Networks*, 174:106250, June 2024. ISSN 0893-6080. doi: 10.1016/j.neunet.2024.106250.

Carlos Riquelme, Joan Puigcerver, Basil Mustafa, Maxim Neumann, Rodolphe Jenatton, André Susano Pinto, Daniel Keysers, and Neil Houlsby. Scaling vision with sparse mixture of experts. In *Adv. Neural Inf. Process. Syst. (NeurIPS)*, volume 34, pp. 8583–8595, 2021.

Jo Schlemper, Jose Caballero, Joseph V. Hajnal, Anthony N. Price, and Daniel Rueckert. A deep cascade of convolutional neural networks for dynamic MR image reconstruction. *IEEE Trans. Med. Imag.*, 37(2):491–503, February 2018. ISSN 1558-254X. doi: 10.1109/TMI.2017.2760978.

Noam Shazeer, Azalia Mirhoseini, Krzysztof Maziarz, Andy Davis, Quoc Le, Geoffrey Hinton, and Jeff Dean. Outrageously large neural networks: The sparsely-gated mixture-of-experts layer, January 2017.

Minghe Shen, Hongping Gan, Chao Ning, Yi Hua, and Tao Zhang. TransCS: A transformer-based hybrid architecture for image compressed sensing. *IEEE Trans. Image Process.*, 31:6991–7005, 2022. ISSN 1941-0042. doi: 10.1109/TIP.2022.3217365.

Minghe Shen, Hongping Gan, Chunyan Ma, Chao Ning, Hongqi Li, and Feng Liu. MTC-CSNet: Marrying transformer and convolution for image compressed sensing. *IEEE Trans. Cybern.*, pp. 1–13, 2024. ISSN 2168-2275. doi: 10.1109/TCYB.2024.3363748.

Jiechong Song and Jian Zhang. SODAS-Net: Side-information-aided deep adaptive shrinkage network for compressive sensing. *IEEE Trans. Instrum. Meas.*, 72:1–12, 2023. ISSN 1557-9662. doi: 10.1109/TIM.2023.3304676.

Jiechong Song, Bin Chen, and Jian Zhang. Deep memory-augmented proximal unrolling network for compressive sensing. *Int. J. Comput. Vis.*, 131(6):1477–1496, June 2023a. ISSN 1573-1405. doi: 10.1007/s11263-023-01765-2.

Jiechong Song, Bin Chen, and Jian Zhang. Dynamic path-controllable deep unfolding network for compressive sensing. *IEEE Trans. Image Process.*, 32:2202–2214, 2023b. ISSN 1941-0042. doi: 10.1109/TIP.2023.3263100.

Jiechong Song, Chong Mou, Shiqi Wang, Siwei Ma, and Jian Zhang. Optimization-inspired cross-attention transformer for compressive sensing. In *IEEE/CVF Conf. Comput. Vis. Pattern Recognit. (CVPR)*, April 2023c.

Liyan Sun, Zhiwen Fan, Yue Huang, Xinghao Ding, and John Paisley. Compressed sensing MRI using a recursive dilated network. In *AAAI Conf. Artif. Intell. (AAAI)*, volume 32, April 2018. doi: 10.1609/aaai.v32i1.11869.

Mengzhu Wang, Jianlong Yuan, and Zhibin Wang. Mixture-of-experts learner for single long-tailed domain generalization. In *ACM Int. Conf. Multimedia (ACM-MM)*, MM '23, pp. 290–299, October 2023. ISBN 9798400701085. doi: 10.1145/3581783.3611871.

Xiaoyang Wang and Hongping Gan. UFC-Net: Unrolling fixed-point continuous network for deep compressive sensing. In *IEEE/CVF Conf. Comput. Vis. Pattern Recognit. (CVPR)*, 2024.

S.J. Wright, R.D. Nowak, and M.A.T. Figueiredo. Sparse reconstruction by separable approximation. *IEEE Trans. Signal Process.*, 57(7):2479–2493, July 2009. ISSN 1053-587X, 1941-0476. doi: 10.1109/TSP.2009.2016892.

Jingfen Xie, Jian Zhang, Yongbing Zhang, and Xiangyang Ji. PUERT: Probabilistic under-sampling and explicable reconstruction network for CS-MRI. *IEEE J. Sel. Top. Signal Process.*, 16(4): 737–749, June 2022. ISSN 1932-4553, 1941-0484. doi: 10.1109/JSTSP.2022.3170654.

Yan Yang, Jian Sun, Huibin Li, and Zongben Xu. Deep ADMM-net for compressive sensing MRI. In D. Lee, M. Sugiyama, U. Luxburg, I. Guyon, and R. Garnett (eds.), *Adv. Neural Inf. Process. Syst. (NeurIPS)*, volume 29, 2016.

Yan Yang, Jian Sun, Huibin Li, and Zongben Xu. ADMM-CSNet: A deep learning approach for image compressive sensing. *IEEE Trans. Pattern Anal. Mach. Intell.*, 42(3):521–538, March 2020. ISSN 0162-8828, 2160-9292, 1939-3539. doi: 10.1109/TPAMI.2018.2883941.

Dongjie Ye, Zhangkai Ni, Hanli Wang, Jian Zhang, Shiqi Wang, and Sam Kwong. CSformer: Bridging convolution and transformer for compressive sensing. *IEEE Trans. Image Process.*, 32: 2827–2842, 2023. ISSN 1941-0042. doi: 10.1109/TIP.2023.3274988.

Hanrong Ye and Dan Xu. TaskExpert: Dynamically assembling multi-task representations with memorial mixture-of-experts. In *IEEE/CVF Int. Conf. Comput. Vis. (ICCV)*, pp. 21828–21837, 2023.

Di You, Jian Zhang, Jingfen Xie, Bin Chen, and Siwei Ma. COAST: Controllable arbitrary-sampling network for compressive sensing. *IEEE Trans. Image Process.*, 30:6066–6080, 2021. ISSN 1941-0042. doi: 10.1109/TIP.2021.3091834.

Xin Yuan. Generalized alternating projection based total variation minimization for compressive sensing. In *IEEE Int. Conf. Image Process. (ICIP)*, pp. 2539–2543, September 2016. doi: 10.1109/ICIP.2016.7532817.

Xin Yuan, David J. Brady, and Aggelos K. Katsaggelos. Snapshot compressive imaging: Theory, algorithms, and applications. *IEEE Signal Process. Mag.*, 38(2):65–88, March 2021. ISSN 1053-5888, 1558-0792. doi: 10.1109/MSP.2020.3023869.

Roman Zeyde, Michael Elad, and Matan Protter. On single image scale-up using sparse-representations. In *Int. Conf. Curves Surfaces*, pp. 711–730, 2012. ISBN 978-3-642-27413-8. doi: 10.1007/978-3-642-27413-8_47.

Zhiyuan Zha, Bihan Wen, Xin Yuan, Saiprasad Ravishankar, Jiantao Zhou, and Ce Zhu. Learning nonlocal sparse and low-rank models for image compressive sensing: Nonlocal sparse and low-rank modeling. *IEEE Signal Process. Mag.*, 40(1):32–44, 2023.

Jian Zhang and Bernard Ghanem. ISTA-Net: Interpretable optimization-inspired deep network for image compressive sensing. In *IEEE Conf. Comput. Vis. Pattern Recognit. (CVPR)*, pp. 1828–1837, June 2018. ISBN 978-1-5386-6420-9. doi: 10.1109/CVPR.2018.00196.

Jian Zhang, Chen Zhao, and Wen Gao. Optimization-inspired compact deep compressive sensing. *IEEE J. Sel. Top. Signal Process.*, 14(4):765–774, May 2020. ISSN 1932-4553, 1941-0484. doi: 10.1109/JSTSP.2020.2977507.

Jian Zhang, Zhenyu Zhang, Jingfen Xie, and Yongbing Zhang. High-throughput deep unfolding network for compressive sensing MRI. *IEEE J. Sel. Top. Signal Process.*, 16(4):750–761, June 2022. ISSN 1941-0484. doi: 10.1109/JSTSP.2022.3170227.

Lei Zhang, Xiaolin Wu, Antoni Buades, and Xin Li. Color demosaicking by local directional interpolation and nonlocal adaptive thresholding. *J. Electron. Imaging*, 20(2):023016, 2011. doi: 10.1117/1.3600632.

Richard Zhang, Phillip Isola, Alexei A. Efros, Eli Shechtman, and Oliver Wang. The unreasonable effectiveness of deep features as a perceptual metric. In *IEEE Conf. Comput. Vis. Pattern Recognit. (CVPR)*, pp. 586–595, June 2018. ISBN 978-1-5386-6420-9. doi: 10.1109/CVPR.2018.00068.

Zhonghao Zhang, Yipeng Liu, Jiani Liu, Fei Wen, and Ce Zhu. AMP-Net: Denoising-based deep unfolding for compressive image sensing. *IEEE Trans. Image Process.*, 30:1487–1500, 2021. ISSN 1057-7149, 1941-0042. doi: 10.1109/TIP.2020.3044472.

Yin-Ping Zhao, Jiancheng Zhang, Yongyong Chen, Zhen Wang, and Xuelong Li. RCUMP: Residual completion unrolling with mixed priors for snapshot compressive imaging. *IEEE Trans. Image Process.*, 33:2347–2360, 2024. ISSN 1941-0042. doi: 10.1109/TIP.2024.3374093.

Hao Zheng, Faming Fang, and Guixu Zhang. Cascaded dilated dense network with two-step data consistency for MRI reconstruction. In *Adv. Neural Inf. Process. Syst. (NeurIPS)*, volume 32, 2019.

Shiyun Zhou, Tingfa Xu, Shaocong Dong, and Jianan Li. RDFNet: Regional dynamic fista-net for spectral snapshot compressive imaging. *IEEE Trans. Comput. Imag.*, 9:490–501, 2023. ISSN 2333-9403. doi: 10.1109/TCI.2023.3237175.

Barret Zoph, Irwan Bello, Sameer Kumar, Nan Du, Yanping Huang, Jeff Dean, Noam Shazeer, and William Fedus. ST-MoE: Designing stable and transferable sparse expert models, April 2022.

A Appendix

In this appendix, we provide more details not covered in the main paper, including:

- Introduction of SpaRSA in Appendix A.1.
- Mathematical descriptions of sampling process for different CI tasks in Appendix A.2;
- Mathematical descriptions of initialization process for different CI tasks in Appendix A.3;
- Implementation specifics of various experiments in Appendix A.4.
- Additional experiments and visualizations in Appendix A.5;
- Limitations of our work in Appendix A.6;
- Code submission and reproducibility in Appendix A.7.

A.1 SpaRSA

SpaRSA (Wright et al. (2009)) (short for **Spa**rse **R**econstruction by **S**eparable **A**pproximation) is a general approach for solving unconstrained optimization problem as follows:

$$\min_{\mathbf{x}} \ \theta(\mathbf{x}) := f(\mathbf{x}) + \tau\gamma(\mathbf{x}), \tag{20}$$

where f is a smooth function, τ is the regularization parameter and γ is always non-smooth and non-convex, which is usually called regularization function and is finite for all $\mathbf{x} \in \mathbb{R}^N$. Specifically, SpaRSA solve Eq. (20) by iterating following equations:

$$\mathbf{x}^{(k+1)} \in \arg\min_{\mathbf{z}} \ (\mathbf{z} - \mathbf{x}^{(k)})\nabla f(\mathbf{x}^{(k)}) + \frac{\lambda}{2}\|\mathbf{z} - \mathbf{x}\|_{\ell 2}^2 + \tau\gamma(\mathbf{z}), \tag{21}$$

where k denotes the k-th iterations and $\lambda \in \mathbb{R}^+$. Notably, the choice of γ can vary, including ℓ_0-norm, ℓ_1-norm, total-variation norm, etc., for different applications, such as image processing and restoration problems. Compared with algorithms that are specially designed for particular tasks, such as ISTA

and FPC, SpaRSA serves as an effective and versatile approach to handle these problems and is computationally competitive. However, being a traditional iterative optimization algorithm, SpaRSA still requires hand-crafted parameter setting, such as λ and τ for different tasks. By incorporating DL modules into SpaRSA, we can fully exploit the potential of powerful generalization ability in SpaRSA with the fast feature learning and correspondence capabilities of DL. Thus, we introduce the deep unfolding SpaRSA as the experts in our proposed DUMoE framework.

A.2 Sampling Process for Different CI Tasks

ICS: Given an input natural image $\mathbf{x} \in \mathbb{R}^{H\times W}$ with height and width of H and W, respectively, image $\mathbf{x}$ is initially partitioned into non-overlapping blocks of size $B \times B$. In cases where the width or height of $\mathbf{x}$ is not perfectly divisible by B, zero-padding is employed to ensure uniform block sizes. These blocks are then transformed into vectors, and a sampling matrix $\mathbf{A} \in \mathbb{R}^{M\times N}$ ($M \ll N$) is applied to yield measurement $\mathbf{y} \in \mathbb{R}^{M}$. In our ICS experiments, $\mathbf{A}$ is initialized as Gaussian matrix. Let $\mathcal{F}_{\text{vec}}(\cdot) : \mathbb{R}^{W\times H} \to \mathbb{R}^{B^2}$ denote the partitioning and vectorization function, and σ represent the sampling ratio, where $M = \lfloor N \times \sigma \rfloor = \lfloor B^2 \times \sigma \rfloor$. The sampling process in ICS can be represented as follows:

$$\mathbf{y} = \mathbf{A}\mathcal{F}_{\text{vec}}(\mathbf{x}). \tag{22}$$

CS-MRI: CS-MRI employs a partial Fourier transform matrix as the sampling matrix $\mathbf{A} = \mathbf{UF}$, where $\mathbf{U}$ represents a sub-sampling mask, and $\mathbf{F}$ corresponds to the Discrete Fourier Transform (DFT). In our CS-MRI experiments, we adopt the Pseudo Radial masks as $\mathbf{U}$. Additionally, the size of $\mathbf{U}$ matches that of the input image $\mathbf{x}$, and σ denotes the ratio between the number of measurement points M and the total number of pixels N in $\mathbf{x}$, i.e., $\sigma = \frac{M}{N}$. The sampling process of CS-MRI is mathematically represented as:

$$\mathbf{y} = \mathbf{Ax} = \mathbf{UFx}. \tag{23}$$

SCI: Consider a 3D hyperspectral image (HSI) $\mathbf{x} \in \mathbb{R}^{H\times W\times N_\zeta}$, where W, H, and N_ζ represent its width, height, and number of wavelengths, respectively. The process begins with the application of a pre-defined coded aperture $\mathbf{A}_\zeta \in \mathbb{R}^{H\times W}$ to modulate the captured HSI, resulting in the transformed HSI denoted as $\mathbf{x}'$:

$$\mathbf{x}'(:,:,n_\zeta) = \mathbf{x}(:,:,n_\zeta) \odot \mathbf{A}_\zeta, \tag{24}$$

where $\odot$ denotes the Hadamard product, and $n_\zeta \in [1, ..., N_\zeta]$ denotes the spectral channels. After modulation, the modulated HSI $\mathbf{x}'$ is subjected to spatial shifts through a disperser, resulting in a transformed measurement $\mathbf{x}'' \in \mathbb{R}^{H\times(W+d(N_\zeta-1))}$. This process induces shear and tilt effects, where d denotes the step of spatial shifting. The dispersion operation can be expressed as:

$$\mathbf{x}''(u, v, n_\zeta) = \mathbf{x}'(x, y + d(\zeta_n - \zeta_c), n_\zeta). \tag{25}$$

Here, ζ_c represents the reference wavelength, ζ_n signifies the wavelength of the n_ζ-th spectral channel, (u, v) denotes the coordinate system on the detector array, and $d(\zeta_n - \zeta_c)$ characterizes the spatial shifting offset of the n_ζ-th channel on $\mathbf{x}''$. As a result, the 2D compressed measurement $\mathbf{y} \in \mathbb{R}^{H\times(W+d(N_\zeta-1))}$ is acquired through the following summation operation:

$$\mathbf{y} = \sum_{n_\zeta=1}^{N_\zeta} \mathbf{x}''(:,:,n_\zeta) + \mathbf{E}. \tag{26}$$

Here, $\mathbf{E}$ signifies the random image noise produced by the photon sensing detector.

A.3 Initialization Process for Different CI Tasks

ICS: For initialization, a matrix multiplication is performed using the transpose of the sampling matrix $\mathbf{A}^T \in \mathbb{R}^{N\times M}$ and $\mathbf{y}$ to obtain a vector of image blocks. Following this, the function $\widetilde{\mathcal{F}}_{\text{vec}}(\cdot) : \mathbb{R}^{B^2} \to \mathbb{R}^{W\times H}$ is applied to recover the image blocks and assemble them into the initial estimate $\mathbf{x}^{(0)}$. This initialization process can be represented as:

$$\mathbf{x}^{(0)} = \widetilde{\mathcal{F}}_{\text{vec}}(\mathbf{A}^T\mathbf{y}). \tag{27}$$

CS-MRI: As for initialization, we apply the inverse DFT, denoted as $\widetilde{\mathbf{F}}$, to the acquired measurement $\mathbf{y}$ to obtain the initial estimate $\mathbf{x}^{(0)}$. Therefore, the initialization of CS-MRI can be expressed as:

$$\mathbf{x}^{(0)} = \widetilde{\mathbf{F}}\mathbf{y}. \tag{28}$$

SCI: Regarding the initialization, we derive $\mathbf{x'}^{(0)} \in \mathbb{R}^{H\times W\times N_\zeta}$ by repeating the measurement $\mathbf{y}$ N_ζ times along the channel dimension. Subsequently, the concatenation of $\mathbf{x'}^{(0)}$ and the 3D mask $\mathbf{A} \in \mathbb{R}^{H\times W\times N_\zeta}$ in channel dimension is inputted into a convolutional layer with a kernel size of 1×1, yielding the initial estimate $\mathbf{x}^{(0)} \in \mathbb{R}^{H\times W\times N_\zeta}$:

$$\mathbf{x}^{(0)} = \mathrm{Conv}_1(\mathrm{Concat}(\mathbf{x'}^{(0)}, \mathbf{A})). \tag{29}$$

A.4 Implementation Details for Different CI Tasks

Table 5: The configurations of pretraining and fine-tuning on the ICS, CS-MRI and SCI tasks.

Configuration	ICS		CS-MRI		SCI	
	Pretrain	Fine-tune	Pretrain	Fine-tune	Pretrain	Fine-tune
sampling matrix init	Gaussian matrix	-	Pseudo Radial mask	-	Pre-defined coded aperture	-
weight init	trunc.normal (0.2)	-	trunc.normal (0.2)	-	trunc.normal (0.2)	-
α_k init	0.5	-	0.5	-	0.5	-
λ_k init	1e-3	-	1e-3	-	1e-3	-
block size	32	32	-	-	-	-
stages count	5	5	5	5	5	5
image size	96×96	96×96	256×256	256×256	256×256	256×256
basic channel count C_0	1	1	1	1	28	28
stage channel count $[C_1, C_2, C_3]$	[32, 48, 80]	[32, 48, 80]	[32, 48, 80]	[32, 48, 80]	[32, 48, 80]	[32, 48, 80]
number of heads N_h	8	8	8	8	8	8
channel per head C_h	64	64	64	64	64	64
batch size	10	10	2	2	2	2
training epochs	400	400	200	100	400	400
base learning rate	2e-4	4e-5	1e-4	4e-5	1e-4	2e-5
min learning rate	1e-6	1e-6	1e-6	1e-6	1e-6	1e-6
optimizer	AdamW (Loshchilov & Hutter (2019))	AdamW	AdamW	AdamW	AdamW	AdamW
weight decay	0.05	0.05	0.05	0.05	0.05	0.05
optimizer momentum	0.9, 0.999	0.9, 0.999	0.9, 0.999	0.9, 0.999	0.9, 0.999	0.9, 0.999
warmup epochs	5	5	5	5	5	5
warmup schedule	linear	linear	linear	linear	linear	linear
learning rate schedule	cosine annealing	cosine annealing	cosine annealing	cosine annealing	cosine annealing	cosine annealing
time consumption	about 5 days	about 5 days	about 30 hours	about 15 hours	about 9 days	about 9 days
implementation	Pytorch 2.2.1 (Paszke et al. (2019))					
CPU	13th Gen Intel Core i9-13900KF					
GPU	RTX 4090 24 GB					

ICS: For the ICS task, we employ a training dataset of 40,000 images randomly selected from the COCO2017 unlabeled image dataset (Lin et al. (2014)), with an additional 1,000 images reserved for validation. During training, we apply diverse data augmentation techniques, including random cropping, scaling, and rotation. Initially, the DUMoE model is trained with a sampling ratio of 0.25. Subsequently, fine-tuning is performed at various sampling ratios, leveraging the pretrained DUMoE weights from the initial training. Notably, the model jointly learns the sampling matrix. Furthermore, LPIPS scores are computed using VGG as the base network (Zhang et al. (2018)).

CS-MRI: In the CS-MRI experiments, our dataset consists of 100 training MRI images and 50 test MRI images sourced from the Brain dataset (Yang et al. (2020)) as used in previous works (Zhang & Ghanem (2018); Yang et al. (2020); Gan et al. (2024a)). All images share a uniform size of 256×256. During training, random rotation is applied as a data augmentation technique. The DUMoE model is first trained with a sampling ratio of 0.10, followed by fine-tuning at various sampling ratios using the pretrained weights.

SCI: The SCI experiments are conducted using both simulation and real HSI data. Following the settings of previous works (Ma et al. (2019); Meng et al. (2020); Huang et al. (2021); Hu et al. (2022); Cai et al. (2022b)), we select $N_\zeta = 28$ wavelengths ranging from 450 nm to 650 nm and $d = 2$ through spectral interpolation manipulation to derive HSIs. For simulations, the CAVE dataset (Park et al. (2007)), which contains thirty-two HSIs with a spatial size of 512×512, serves as the training set, while ten scenes from KAIST (Choi et al. (2017)) are utilized for testing. During training, data augmentation techniques such as random cropping into 256×256, slicing, and rotation are employed. In real data experiments, 11-bit shot noise is introduced into the measurements of CAVE and KAIST datasets during training to mimic real-world noise disturbances. Fine-tuning is performed based on the pretrained model using simulation data. Testing is conducted using five real scenes from the real CASSI system (Meng et al. (2020)).

Please refer to Tab. 5 for detailed configurations of DUMoE for the ICS, CS-MRI and SCI tasks.

Table 6: Average PSNR (dB) and SSIM performance comparisons of DUMoE and other ICS methods on various datasets at high sampling ratios (0.30, 0.40 and 0.50).

Methods	Urban100								General100							
	0.30		0.40		0.50		Avg.		0.30		0.40		0.50		Avg.	
	PSNR	SSIM	PSNR	SSIM	PSNR	SSIM	PSNR	SSIM	PSNR	SSIM	PSNR	SSIM	PSNR	SSIM	PSNR	SSIM
CASNet (TIP 2022)	33.35	0.9509	35.46	0.9668	37.46	0.9773	35.42	0.9650	39.32	0.9730	41.56	0.9827	43.74	0.9887	41.54	0.9815
DGUNet$^+$ (CVPR 2022)	33.16	0.9510	35.24	0.9666	37.65	0.9785	35.35	0.9654	38.87	0.9724	41.07	0.9821	43.26	0.9884	41.07	0.9810
FSOINet (ICASSP 2022)	33.84	0.9540	35.93	0.9688	37.80	0.9777	35.86	0.9668	39.40	0.9735	41.62	0.9831	43.69	0.9887	41.57	0.9818
TransCS (TIP 2022)	32.01	0.9384	35.29	0.9649	37.28	0.9762	34.86	0.9598	37.81	0.9669	40.74	0.9806	42.89	0.9873	40.48	0.9782
DPC-DUN (TIP 2023)	33.53	0.9449	35.58	0.9622	37.52	0.9737	35.54	0.9603	37.76	0.9590	39.95	0.9731	42.00	0.9820	39.91	0.9713
OCTUF (CVPR 2023)	34.21	0.9555	36.25	0.9669	38.29	0.9797	36.25	0.9674	39.54	0.9740	41.76	0.9833	43.95	0.9892	41.75	0.9822
NesTD-Net (TIP 2024)	33.52	0.9516	35.96	0.9683	38.07	0.9786	35.85	0.9662	39.34	0.9732	41.78	0.9831	43.97	0.9891	41.70	0.9818
LTwIST (TCSVT 2024)	33.02	0.9477	35.16	0.9643	37.12	0.9753	35.10	0.9624	38.61	0.9699	40.85	0.9806	42.97	0.9872	40.81	0.9792
UFC-Net (CVPR 2024)	33.78	0.9524	35.93	0.9679	37.98	0.9782	35.90	0.9662	38.89	0.9704	41.17	0.9810	43.35	0.9878	41.14	0.9797
DUMoE (Our Method)	**34.54**	**0.9576**	**36.58**	**0.9706**	**38.49**	**0.9797**	**36.54**	**0.9693**	**39.64**	**0.9743**	**41.96**	**0.9836**	**44.09**	**0.9894**	**41.90**	**0.9824**

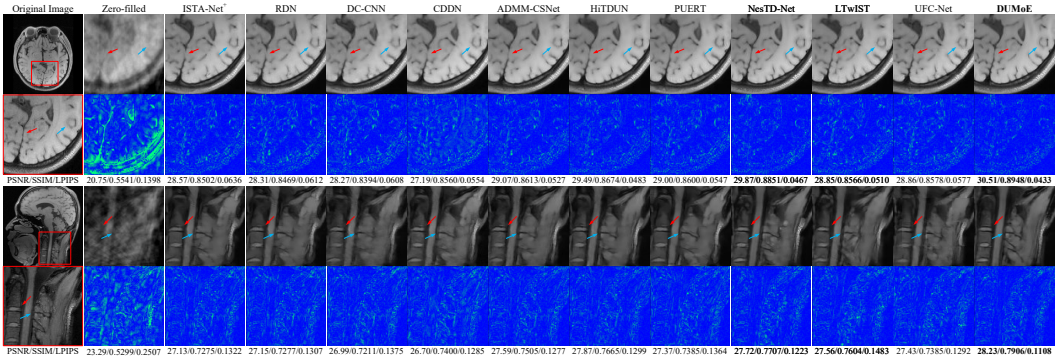

Figure 6: Comparisons of visual results with error maps and corresponding PSNR (dB)/SSIM/LPIPS performance between DUMoE and other advanced CS-MRI methods at a sampling ratio of 0.10.

A.5 Additional Experiments

A.5.1 ICS

We conduct qualitative comparisons between DUMoE and other ICS methods on Urban100 and General100 at high sampling ratios (0.30, 0.40, and 0.50). As shown in Tab. 6, our proposed DUMoE consistently outperforms other advanced methods at these high sampling ratios, with OCTUF and NesTD-Net achieving the second-best results. Specifically, on Urban100 at a sampling ratio of 0.30, DUMoE achieves PSNR improvements of approximately 1.01 dB (3.02%), 0.33 dB (0.96%), 1.52 dB (4.60%), 1.02 dB (3.04%), and 0.76 dB (2.25%) compared to DPC-DUN, OCTUF, LTwIST, NesTD-Net, and UFC-Net, respectively. Additionally, the SSIM improvements are approximately 0.0127 (1.34%), 0.0021 (0.22%), 0.0099 (1.04%), 0.0060 (0.63%), and 0.0052 (0.55%), respectively.

A.5.2 CS-MRI

We present visual comparisons of reconstructed magnetic resonance (MR) images between DUMoE and other CS-MRI methods. As shown in Fig. 6, DUMoE exhibits superior performance in reconstructing fine details and enhancing human perception quality, with fewer errors compared to other methods in CS-MRI tasks.

A.5.3 SCI

We present visual comparisons of reconstructed HSI between DUMoE and other SCI methods using both simulated and real HSI data. As illustrated in Fig. 7, the reconstructed HSI by DUMoE exhibits fewer artifacts and more accurate details compared to other SCI methods across various spectral channels. Additionally, the spectral density curves in the bottom left of Fig. 7, corresponding to the areas highlighted in the red boxes in the RGB image, demonstrate the highest correlation and alignment of DUMoE's spectral curves with the reference curves, highlighting the advantages of our proposed DUMoE in HSI reconstruction. Furthermore, Fig. 8 presents visual comparisons of DUMoE and other SCI methods on Scene 4 and Scene 5 using 2 spectral channels of real HSI data

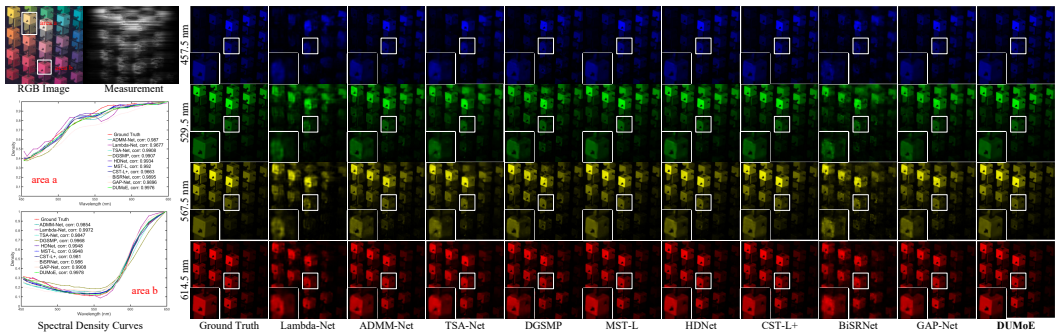

Figure 7: Simulation HSI reconstruction comparisons of DUMoE and other SCI methods on Scene 2 with 4 (out of 28) spectral channels.

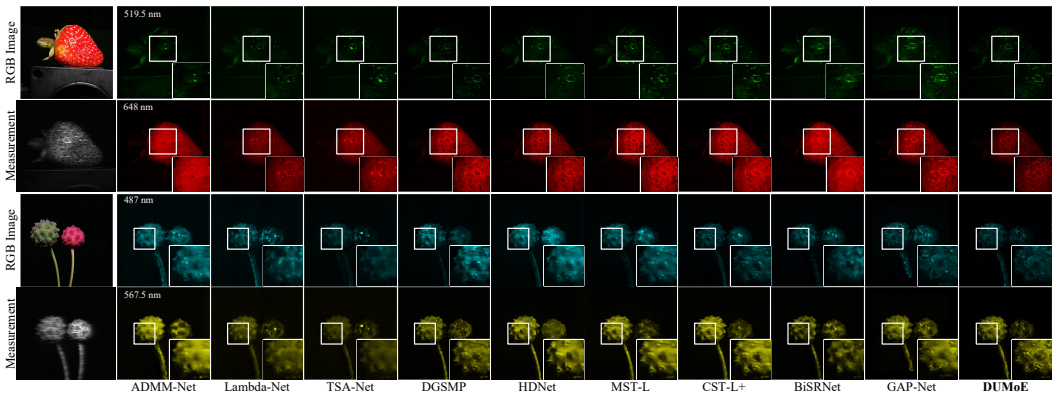

Figure 8: Real HSI reconstruction comparisons of DUMoE and other SCI methods on Scene 4 and Scene 5 with 2 (out of 28) spectral channels.

(Meng et al. (2020)), showcasing the superior performance of DUMoE on real HSI data. Moreover, Tab. 7 provides details on the number of parameters and FLOPs of different SCI methods on the KAIST dataset (Choi et al. (2017)).

Table 7: Number of parameters (M) and FLOPs (G) of different SCI methods on the KAIST dataset.

Methods	ADMM-Net	Lambda-Net	TSA-Net	DGSMP	HDNet	MST-L	CST-L+	RDFNet	GAP-Net	EDUNet	DWMT	DUMoE
Params.	4.27	62.64	44.25	3.76	2.37	2.03	3.00	1.29	4.27	1.51	14.48	4.07
FLOPs	78.58	117.98	110.06	646.65	154.76	28.15	40.01	604.88	78.58	24.24	46.71	183.30

A.5.4 Visualizations of DAM for Various CI Tasks

In this section, we present detailed visualizations of Degradation-Aware Mask (DAM) for three CI tasks. Specifically, we illustrate how DAM captures different types of degradation at the image-level domain $\mathbf{d}_1^{(k)}$, the measurement-level domain $\mathbf{d}_2^{(k)}$, and how the absolute sum of generated mask channels evolves across stages $k = 1, 3, 5$.

In ICS, as shown in Fig. 9, the image-level domain degradation $\mathbf{d}_1^{(k)}$ primarily reflects global image degradation and block artifacts, which are characteristic of the block sampling process in compressed sensing. Conversely, $\mathbf{d}_2^{(k)}$ is more focused on finer details such as edges and noise, which tend to be more vulnerable to degradation. As the number of stages increases, the mask progressively incorporates richer texture details.

For CS-MRI, as shown in Fig. 10, sampling is performed in the Fourier domain using a subsampling mask, resulting in aliasing artifacts. Here, both $\mathbf{d}_1^{(k)}$ and $\mathbf{d}_2^{(k)}$ capture different aspects of this

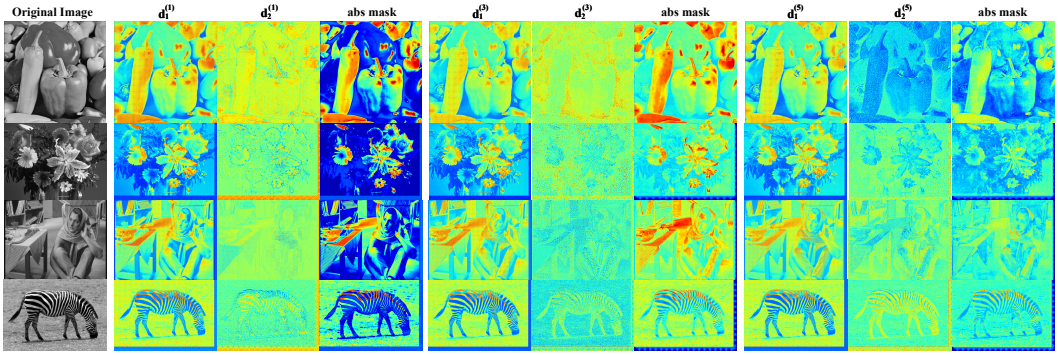

Figure 9: The visualizations of image-level domain degradation $\mathbf{d}_1^{(k)}$, measurement-level domain degradation $\mathbf{d}_2^{(k)}$ and absolute sum of generated mask channels at stages of $k = \{1, 3, 5\}$ for ICS at a sampling ratio of 0.25.

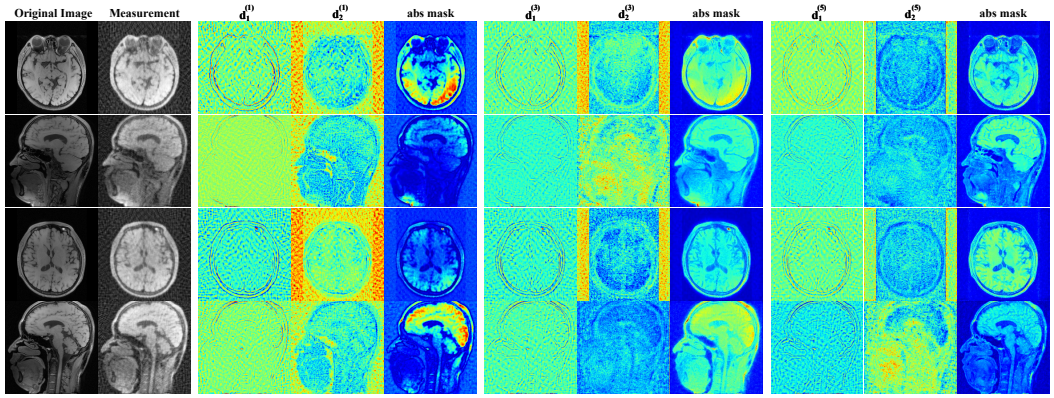

Figure 10: The visualizations of image-level domain degradation $\mathbf{d}_1^{(k)}$, measurement-level domain degradation $\mathbf{d}_2^{(k)}$ and absolute sum of generated mask channels at stages of $k = \{1, 3, 5\}$ for CS-MRI at a sampling ratio of 0.20.

degradation: $\mathbf{d}_1^{(k)}$ emphasizes edge information, while $\mathbf{d}_2^{(k)}$ focuses on broader degraded regions. The mask also becomes more refined with stage progression, revealing increasing detail.

The SCI task, as shown in Fig. 11, involves a 3D hyperspectral image compressed into a 1D measurement via a coded aperture. This process is prone to noise-induced artifacts. Initially, both

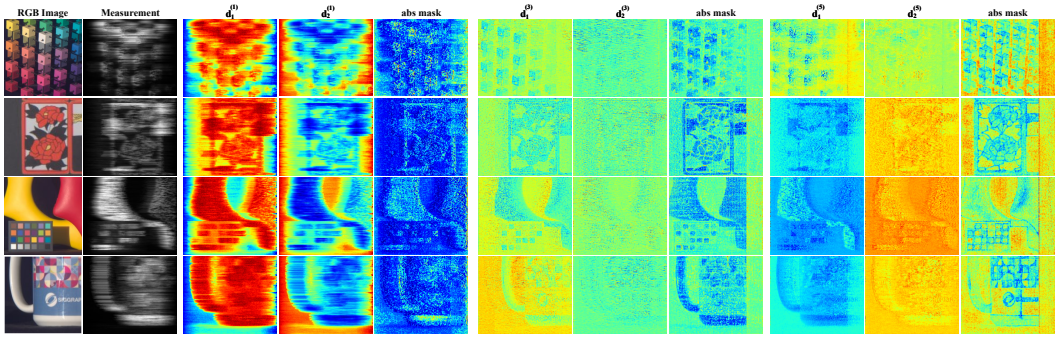

Figure 11: The visualizations of image-level domain degradation $\mathbf{d}_1^{(k)}$, measurement-level domain degradation $\mathbf{d}_2^{(k)}$ and absolute sum of generated mask channels at stages of $k = \{1, 3, 5\}$ for SCI.

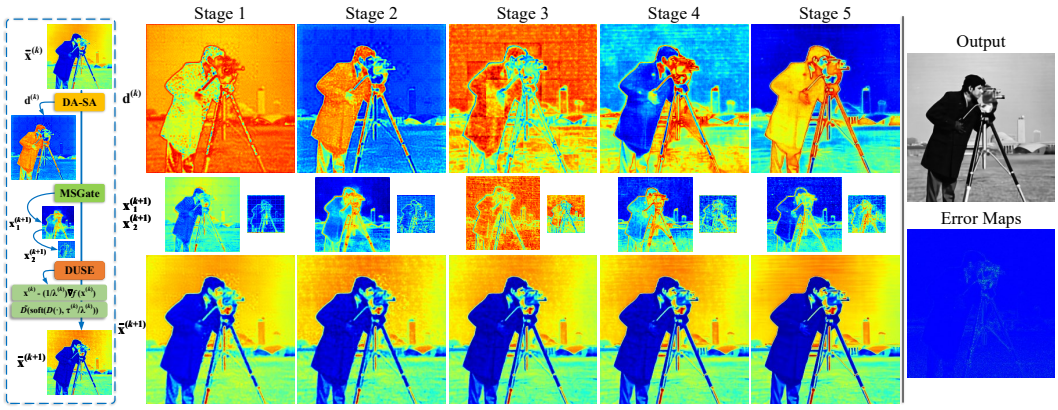

Figure 12: Feature visualization of the iteration stages in DUMoE at a sampling ratio of 0.10.

$\mathbf{d}_1^{(k)}$ and $\mathbf{d}_2^{(k)}$ capture these artifacts, but as the stages evolve, $\mathbf{d}_1^{(k)}$ emphasizes texture recovery, while $\mathbf{d}_2^{(k)}$ continues to highlight noise-affected areas. The mask becomes more precise in revealing important details as the stages progress.

As detailed in Fig. 5a, Tab. 4a and through the analysis in Sec. 5.1 of our paper, the DAM effectively guides DUMoE to focus on critical degraded image areas and fine details, despite variations in sampling, initialization processes, and data types (2D and 3D) across different CI tasks. This highlights the effectiveness and generalization of our proposed method, enhancing feature extraction capabilities across diverse CI tasks.

A.5.5 Visualizations of Image Feature Maps

Fig. 12 visualizes the features across different iteration stages and modules in DUMoE, demonstrating the contributions and attention of different modules to the iterative image refinement during the reconstruction, thus enhancing the effectiveness of DUMoE.

Furthermore, as shown in Fig. 13, we present visualizations of image features and the corresponding top-1 selection of the DUSE for different images at each iteration stage across various sampling ratios. In the initial stages, DUMoE tends to capture the overall contour information of the images. However, at lower sampling ratios, block artifacts may be more prominent. Nevertheless, as the iterative stages progress, the details and texture information within the images become increasingly enriched, consequently diminishing block artifacts and resulting in high-fidelity image reconstruction. Notably, it is evident that at different sampling ratios, the refinement and enhancement of details and texture information in diverse images evolve through different experts during the iterative stages. This observation underscores the ability of DUMoE to dynamically select DUSE, facilitating iterative refinement tailored to the diverse characteristics of images during the iteration stages.

A.5.6 Ablation Studies on DUSE Number

Table 8: The performance comparisons of cases under different number of DUSE.

DUSE	1	2	3	5	3
Switch Routing	-	w/	w/	w/	w/o
PSNR (dB)	34.31	34.39	34.42	34.38	34.39
SSIM	0.9325	0.9332	0.9334	0.9332	0.9329
Params. (M)	3.99	4.08	4.17	4.34	4.17
FLOPs (G)	142.34	142.34	142.34	142.34	158.72

We conduct an ablation study on the number of experts as shown in Tab. 8. As the number of DUSE increases, performance gradually improves, peaking at three blocks. However, performance declines

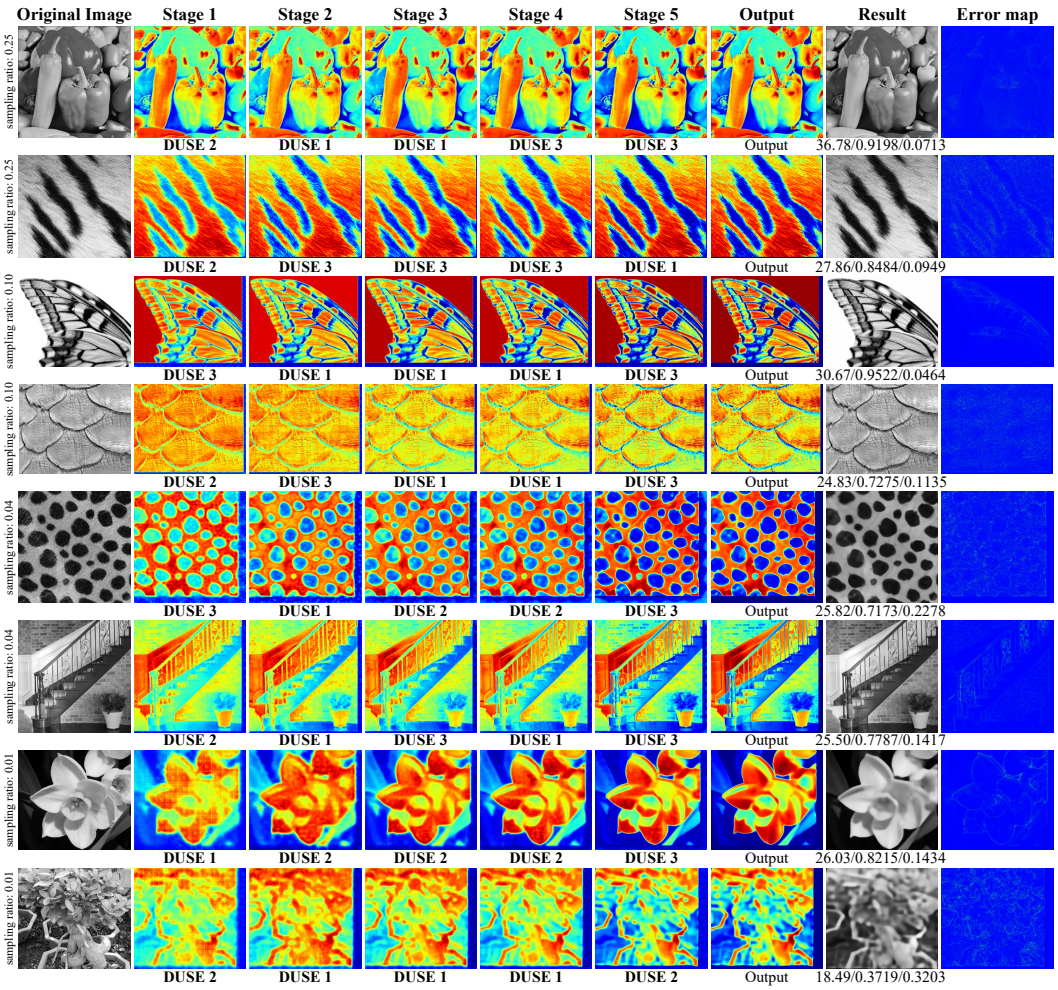

Figure 13: Visualizations of image features and the corresponding top-1 selection of the DUSE for diverse images in each iteration stage at different sampling ratios.

when the number of DUSE reaches five, likely due to increased training complexity and the higher number of parameters, requiring more epochs to achieve optimal performance.

A.6 LIMITATIONS

In our main paper, we primarily focus on utilizing the ℓ_1-norm as the image prior to enforce sparsity in the transform domain and employ soft thresholding to address Eq. (8). However, it's worth noting that various other image priors exist, including the ℓ_0-norm, total variation, low-rank, etc., for different applications. Besides, many deep unfolding-based methods leverage deep denoising networks to replace image prior terms (Song et al. (2023c); Mou et al. (2022); Cai et al. (2022c)). Moving forward, we aim to explore a broader spectrum of image prior terms, thereby enhancing the versatility of DUMoE to address a wider array of image ill-posed problems, such as image super-resolution, image deraining, image denoising, etc.

Furthermore, the proposed DUMoE framework is designed as a general approach capable of addressing a broad range of CI tasks, including ICS, CS-MRI, and SCI, without being restricted to a single domain. This generality allows DUMoE to be applied to various CI tasks with diverse data characteristics (e.g., 2D and 3D) and requirements (e.g., different sampling and initialization processes). However, this broad applicability may result in performance trade-offs for highly specialized tasks. We view this as an area for future improvement, where incorporating more specialized knowledge into the DUMoE framework could potentially mitigate these trade-offs and yield more competitive results in specialized applications.

A.7 CODE SUBMISSION AND REPRODUCIBILITY

We submit the source code and pre-trained models in the supplemental material and provide the detailed experimental settings for reproducing the results presented in our paper. Additionally, both the source code and pre-trained models will be publicly released for broader accessibility and reproducibility.